Geochemistry Geophysics Geosystems G3
AN ELECTRONIC JOURNAL OF THE EARTH SCIENCES
Published by AGU and the Geochemical Society

*Article*
Volume 11
9 January 2010
Q0AB03, doi:10.1029/2009GC002637
ISSN: 1525-2027



# Imaging detailed crustal structure and magmatic intrusion across the Ethiopian Rift using a dense linear broadband array

**D. G. Cornwell**
*Department of Geology, University of Leicester, University Road, Leicester LE1 7RH, UK*

*Now at School of Earth and Environment, University of Leeds, Woodhouse Lane, Leeds LS2 9JT, UK (d.cornwell@see.leeds.ac.uk)*

**P. K. H. Maguire and R. W. England**
*Department of Geology, University of Leicester, University Road, Leicester LE1 7RH, UK (pkm@le.ac.uk; rwe5@le.ac.uk)*

**G. W. Stuart**
*School of Earth and Environment, University of Leeds, Woodhouse Lane, Leeds LS2 9JT, UK (g.stuart@see.leeds.ac.uk)*

[1] Continental rifting is constrained by the architecture and heterogeneous composition of lithosphere within which rifting occurs. Recent studies in Ethiopia show that the Cenozoic northern Main Ethiopian Rift (NMER) has developed in a Neoproterozoic lithospheric framework modified by a Tertiary plume, magma injection having replaced mechanical failure as the main strain accommodation mechanism. A 400 km long profile of 91 broadband seismic stations striking southeast across the NMER from the uplifted Ethiopian plateau to beyond the southern margin of the rift has provided a high-resolution *P* receiver function section, here interpreted in terms of crustal architecture and composition in light of independent geophysical observations. Synrift deposits are identified over a ~110 km wide region beneath which strain was accommodated during the early stages of rifting. Major variations in crustal thickness and seismic properties along the profile divide the crust into four distinct regions. Beneath the northwestern rift flank (average crustal thickness 37.5 km and $V_p/V_s$ 1.82) mafic middle and lower crustal rocks are overlain by a felsic upper crust. Here a high *P* wave velocity lowest crustal layer (northwestern lower crustal layer) is proposed to consist of frozen gabbroic sills and possibly some partial melt. We suggest partial melting of lower crustal rocks and/or fractional crystallization may have contributed to the bimodal prerift and synrift magmatism. Also, the presence of this layer through its effect on crustal and lithospheric strength and rift-related diking may have controlled the location and development of the NMER in the vicinity of the profile. Beneath the rift (average crustal thickness 34.5 km and $V_p/V_s$ 1.87) the crust is subdivided into a northwestern sector, with a thinned crust and strong likelihood of partially molten rocks, and a southeastern sector, where high velocity and density anomalies and the presence of a Moho "hole" in the receiver function profile constrain the limits of a well-developed crustal magma system. To the southeast, a 35 km wide zone marks the transition from intruded and thinned (by ~5 km) crust beneath the rift to the amagmatic, thick crust of the southeastern rift flank (average crustal thickness 39 km and $V_p/V_s$ 1.77) suggested to be of felsic to intermediate composition.

**Components:** 3220 words, 9 figures, 4 tables.

**Keywords:** crustal structure; underplate; rifting; receiver function; magma intrusion; Ethiopia.

**Index Terms:** 8178 Tectonophysics: Tectonics and magmatism; 7205 Seismology: Continental crust (1219); 9305 Geographic Location: Africa.

**Received** 19 May 2009; **Revised** 29 September 2009; **Accepted** 5 October 2009; **Published** 9 January 2010.

Cornwell, D. G., P. K. H. Maguire, R. W. England, and G. W. Stuart (2010), Imaging detailed crustal structure and magmatic intrusion across the Ethiopian Rift using a dense linear broadband array, *Geochem. Geophys. Geosyst.*, *11*, Q0AB03, doi:10.1029/2009GC002637.

**Theme:** Magma-Rich Extensional Regimes

**Guest Editors:** R. Meyer, J. van Wijk, A. Breivik, and C. Tegner

## 1. Introduction

[2] Continental rifts often evolve in settings with heterogeneous crust and lithosphere [e.g., *Jones et al.*, 1992; *Birt et al.*, 1997; *Wilson et al.*, 2005]. The heterogeneity may be added as the rift develops, such as the addition of magmatic material to the crust [e.g., *Thybo et al.*, 2000; *White et al.*, 2008; *Thybo and Nielsen*, 2009], or it may be preexisting, influencing the location, style and timing of the rift [e.g., *Dunbar and Sawyer*, 1989; *Tommasi and Vauchez*, 2001; *van Wijk and Blackman*, 2005; *Huismans and Beaumont*, 2007].

[3] The Main Ethiopian Rift (MER) provides an excellent natural laboratory to study such heterogeneity associated with continental rift zones as it initiated in a Precambrian lithospheric fabric that had been modified by Tertiary plume magmatism [*Gashawbeza et al.*, 2004; *Keranen and Klemperer*, 2008] and then evolved into the present-day rift, in which magma injection has probably replaced mechanical failure as the main strain accommodation mechanism [*Ebinger and Casey*, 2001]. Furthermore, the region is well studied; previous geophysical studies have revealed first-order cross-rift and along-axis changes in crustal and/or upper mantle velocity [*Keranen et al.*, 2004; *Mackenzie et al.*, 2005; *Bastow et al.*, 2005; *Benoit et al.*, 2006a, 2006b; *Maguire et al.*, 2006], density [*Mahatsente et al.*, 1999; *Woldetinsae and Götze*, 2005; *Cornwell et al.*, 2006] and electrical conductivity [*Whaler and Hautot*, 2006].

[4] The present paper provides increased lateral resolution by constraining small-scale (<50 km) changes in seismic crustal structure and inferred composition beneath the rift and its uplifted flanks using receiver functions from a dense (~5 km spacing) 400 km cross-rift profile of broadband seismometers. These seismological data span the northern MER (NMER) and form part of the multidisciplinary Ethiopia Afar Geoscientific Lithospheric Experiment (EAGLE) [*Maguire et al.*, 2003]. Receiver functions (RFs) [e.g., *Langston*, 1977] are analyzed to (1) constrain the crustal structure beneath the rift valley and rift flanks, (2) define the thickness and extent of magmatic addition to the crust, and (3) infer the composition of the crust and both hot spot– and rift-related magmatic addition. The implications of these new results are explored in terms of rift evolution and the effects of magma emplacement.

### 1.1. Geology and Tectonics

[5] The NMER formed within the Precambrian crustal basement of the Pan-African shield that consists of Neoproterozoic orogenic belts such as the Arabian-Nubian shield (ANS) [*Stern*, 1994; *Abdelsalam and Stern*, 1996; *Johnson and Woldehaimanot*, 2003]. The ANS is largely composed of juvenile calc-alkaline volcanic rocks which have suffered low-grade metamorphism during closure of sutures incorporating ophiolitic assemblages [*Abdelsalam and Stern*, 1996; *Yihunnie and Tesfaye*, 2002]. The region is covered by in excess of 3 km of Jurassic to Late Eocene marine sediments that were deposited unconformably on the Precambrian basement [*Dow et al.*, 1971; *Garland*, 1972; *Tefera et al.*, 1996] (Figure 1).

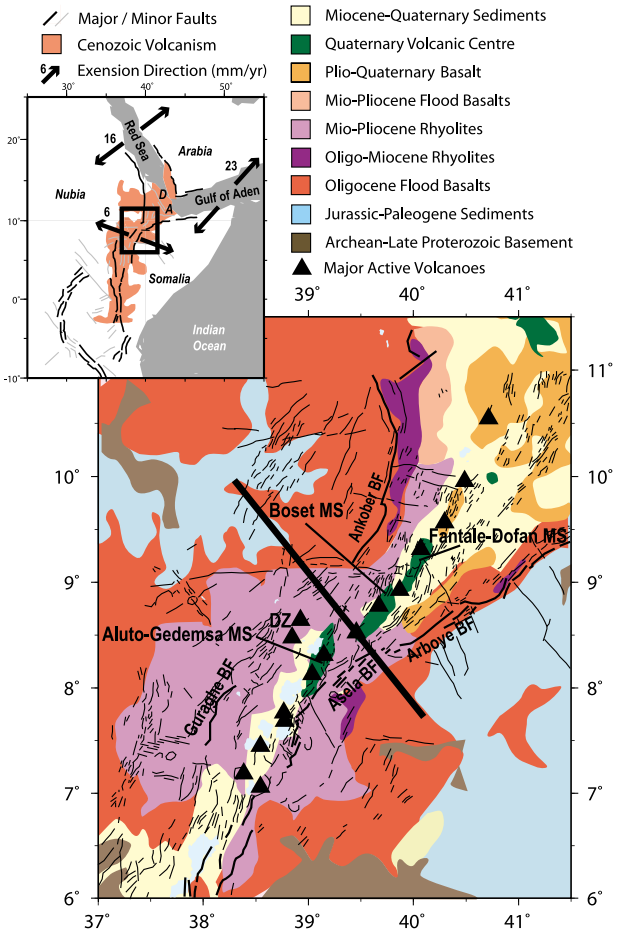


**Figure 1.** A simplified geological and structural map of the northern main Ethiopian rift with magmatic segments (MS) and border faults (BF) [after *Boccaletti et al.*, 1999; *Ebinger and Casey*, 2001; *Acocella and Korme*, 2002; *Korme et al.*, 2004; *Wolfenden et al.*, 2004]. The location of Debre Zeit (Bishoftu) is shown as DZ and the bold line indicates the best fit EAGLE Line 1 profile [e.g., *Maguire et al.*, 2003]. The inset shows the tectonic setting of the northern East African rift system with major fault lineation, volcanism and extension rates, and directions between tectonic plates [*Bilham et al.*, 1999; *Chu and Gordon*, 1999; *McClusky et al.*, 2003]. The location of Danakil (D) and the Asal rift (A) are also shown. Adapted from *Cornwell et al.* [2006].

[6] A hot mantle upwelling impacting onto the base of the lithosphere is believed to have initiated volcanism in southwestern Ethiopia (~45–40 Ma [*Ebinger et al.*, 1993]) and in northern Ethiopia where flood basalts cover an area of about 600,000 km$^2$ [*Mohr*, 1983] and consist of a <2 km layer of bimodal basalt-rhyolite volcanic rocks [e.g., *Ayalew et al.*, 2002; *Ayalew and Yirgu*, 2003]. The flood basalts are thought to have erupted very rapidly (within 1 Myr) throughout northern Ethiopia at ~30 Ma [*Hofmann et al.*, 1997; *Rochette et al.*, 1998; *Coulie et al.*, 2003], but the ages of prerift basalts have been measured at ~24 Ma in the NMER [*Chernet et al.*, 1998]. Uplift of the Ethiopian Plateau followed the flood basalt eruption from 29 to 25 Ma [*Pik et al.*, 2003] and possibly continued episodically to the present day [*Gani et al.*, 2007].

[7] Rifting within the southern and central MER is believed to have occurred between 18 and 15 Ma [*WoldeGabriel et al.*, 1990] with extension in the NMER commencing after ~11 Ma with the development of border faults and half grabens [*Ebinger and Casey*, 2001; *Wolfenden et al.*, 2004]. The present-day rift floor of the NMER is characterized by elongate axial zones of Quaternary eruptive centers arranged in an en echelon right-stepping pattern that developed after 1.8 Ma [*Boccaletti et al.*, 1999; *Ebinger and Casey*, 2001] (Figure 1).

[8] Geochemical analysis indicates that synrift basalts were derived by moderate degrees of melting of fertile peridotite at depths probably corresponding to the base of the modern lithosphere (53–88 km) [*Rooney et al.*, 2005]. Three compositionally distinct source domains were identified, based upon mixing of melts: (1) a depleted upper mantle source, (2) an enriched mantle source with an upper crustal component, and (3) an enriched mantle source with an lower crustal component [*Furman et al.*, 2006]. Quaternary xenolith-bearing basalts from the Debre Zeit (Bishoftu) (Figure 1) and Butajira regions, offset 20 km to the west of the contemporaneous main rift axis, show that a process of diking/veining affects the crust and lithospheric mantle in the NMER to a depth of at least 30 km [*Rooney et al.*, 2005]. Plio-Holocene fluvio-lacustrine sediments and Holocene alluvial cover comprise the remainder of the rift valley fill [e.g., *Kazmin*, 1975; *Abebe et al.*, 2005].

## 1.2. Previous Seismological Crustal Studies

### 1.2.1. Controlled Source Seismic Methods

[9] As part of the EAGLE project across- and along-rift ~400 km long wide-angle reflection/refraction controlled source profiles were shot, together with a 100 km diameter 2-D array spanning the rift valley at the intersection of the two profiles [*Maguire et al.*, 2003]. Traveltimes were modeled using a combination of tomography and forward modeling to produce 2-D and 3-D *P* wave velocity models for the crust and uppermost mantle

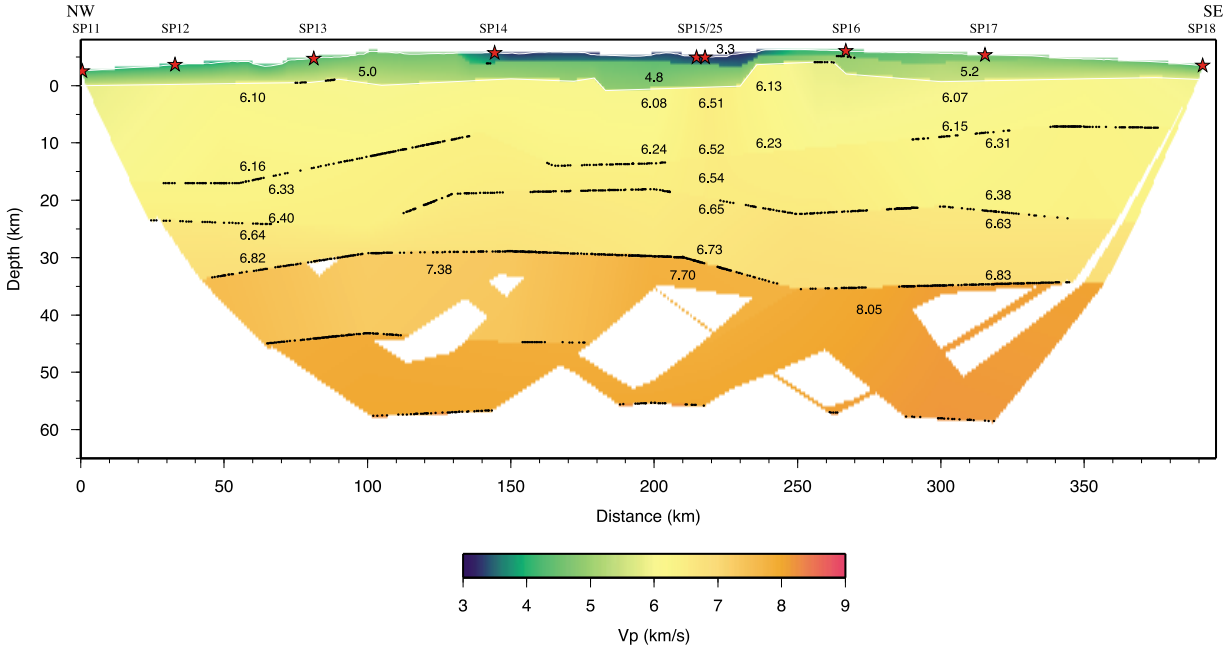


**Figure 2.** Ray trace *P* wave velocity model for the EAGLE cross-rift controlled source seismic study (after *Mackenzie et al.* [2005], ©2005, Wiley-Blackwell). Model outlines indicate regions sampled by raypaths, and *P* wave velocities are given in km/s. Bold lines mark horizons sampled by reflected rays, and SP denotes shot point location.

[*Keranen et al.*, 2004; *Mackenzie et al.*, 2005; *Maguire et al.*, 2006].

[10] An overview by *Maguire et al.* [2006] identifies two main results related to the cross-rift profile (Figure 2): (1) middle and upper crust velocities varying from ~6.1 km/s beneath the rift flanks to ~6.6 beneath axial zones of intense Quaternary volcanic activity, interpreted as cooled gabbroic bodies arranged en echelon along the current rift axis, and (2) a high-velocity ($V_p \approx 7.4$ km/s) lower crustal layer beneath the northwestern rift flank, interpreted as Oligocene mafic material emplaced at the base of the crust (underplate).

### 1.2.2. Teleseismic Earthquake Analyses

[11] Controlled-source seismic methods provide *P* wave velocity ($V_p$) information of the subsurface from predominantly horizontally traveling, high-frequency waves. Teleseismic RF studies, on the other hand, provide *S* wave velocity ($V_s$) information from vertically traveling waves and therefore have the ability to define lateral and depth-wise changes in subsurface composition via the ratio of $V_p$ to $V_s$ ($V_p/V_s$).

[12] Table 1 summarizes the results of previous RF studies in Ethiopia, all of which used the $H$-$\kappa$ stacking method of analysis [*Zhu and Kanamori*, 2000] to estimate crustal thickness and bulk crustal $V_p/V_s$. *Ayele et al.* [2004] analyzed RFs at the permanent broadband stations in Addis Ababa (FURI and AAE) to find a crustal thickness of ~40 km. *Dugda et al.* [2005] deduce that the crust within the NMER is of mafic composition where $V_p/V_s \approx 1.87$ and partial melt may exist where $V_p/V_s > 1.87$. They attribute the large range in crustal thickness beneath rift stations (Table 1) to differing amounts of extension and/or underplating and intrusion. Outside of the rift, the estimated Moho depths and $V_p/V_s$ values of 1.71–1.81 were interpreted to represent crust that has not been modified greatly by Cenozoic rifting and volcanism.

[13] *Stuart et al.* [2006] use a more dense array to find similar estimates of average crustal $V_p/V_s$ and Moho depth to *Dugda et al.* [2005] within the rift, and interpret a mafic crust and the presence of partial melt (where $V_p/V_s > 1.95$) toward the Afar depression. They also note high $V_p/V_s$ values of more than 2.0 beneath the western rift margin. The western flank of the rift (Nubian plate) generally displays a thicker crust (40–43 km) than the eastern flank (Somalian plate) (38–40 km).

[14] This study reports on a RF study along a 400 km long profile that spans the NMER with station spacing of the order of 5 km (Figure 3). The

**Table 1.** A Summary of the Findings of Previous Receiver Function Studies in Ethiopia and Djibouti[a]

| Region | Moho Depth (km) | $V_p/V_s$ | Poisson's Ratio ($\sigma$) | Source |
|---|---|---|---|---|
| Djibouti | 23 | 1.90 | 0.31 | D06 |
| Afar | 25 | 2.13 | 0.36 | D05 |
| MER | 27–38 | 1.78–2.08 | 0.27–0.35 | D05 |
| MER | 30–38 | 1.85–2.10 | 0.29–0.35 | S06 |
| E. Plateau | 37–42 | 1.74–1.81 | 0.25–0.28 | D05 |
| E. Plateau | 38–40 | ~1.80 | ~0.26 | S06 |
| W. Plateau | 34–44 | 1.71–1.81 | 0.24–0.28 | D05 |
| W. Plateau | 38–43 | ~1.85 | ~0.28 | S06 |

[a] MER, Main Ethiopian Rift; E. Plateau, the Ethiopian Plateau region to the east of the MER; W. Plateau, the Ethiopian Plateau region to the west of the MER. The $V_p/V_s$ and Poisson's ratio values are given for each study for comparison. D05, *Dugda et al.* [2005]; D06, *Dugda and Nyblade* [2006]; S06, *Stuart et al.* [2006].

45 EAGLE broadband stations that *Stuart et al.* [2006] used to calculate RFs were also included (e.g., BORE, E51).

## 2. Method

### 2.1. Data

[15] RFs were calculated using data recorded by EAGLE phase I, II and III broadband stations [*Maguire et al.*, 2003]. The broadband data from phase III are previously unpublished and were recorded by an installation of 91 SEIS-UK Güralp CMG-6TD three-component broadband seismometers for a period of 2 months (21 November 2002 to 19 January 2003) along the 400 km cross-rift profile (Figure 3).

[16] The individual recordings of earthquakes ($m_b >$ 4.5, angular distances of 29–100°) from the NEIC catalogue were visually inspected across the phase III profile; a total of 22 events (Table 2) displayed a clear *P* arrival with high signal-to-noise and were accepted for further analysis. The events used for the phase I and II arrays RF analysis were listed by *Bastow* [2005].

### 2.2. Receiver Function Calculation

[17] RFs record the seismic response to an incoming teleseismic *P* wave at a given seismometer. *P-S* conversions caused by any interface with a significant acoustic impedance contrast occur as peaks on RFs, at times related to their depth beneath the recording seismic station. Vertically polarized converted *S* waves dominate the radial component of a RF (*R*) whereas horizontally polarized converted *S* waves dominate the transverse component (*T*).

[18] Following the removal of instrument responses, RFs were calculated using the spectral division method [*Ammon*, 1991] with a water level fraction of 0.001 and Gaussian width parameters of either 1.0 or 2.0 (≃0.5 or 1 Hz low-pass filters). A RF was only accepted if it satisfies the following criteria under visual examination: (1) the result of deconvolving the vertical (*Z*) component from itself, using the chosen Gaussian width, shows a narrow, undistorted pulse; (2) the *R* and *T* RFs do not show significant presignal noise; (3) the *T* RFs show smaller (or comparable) amplitudes to the *R* RF; (4) the direct *P* arrival energy peak on the *R* RF occurs at, or shortly after, zero time; and (5) the *R* and *T* RFs do not display significant "ringing."

[19] Approximately a third of the calculated RFs exhibited a long-period (>20–30 s) noise signature, regardless of the choice of Gaussian width and water level fraction, which was removed by applying a

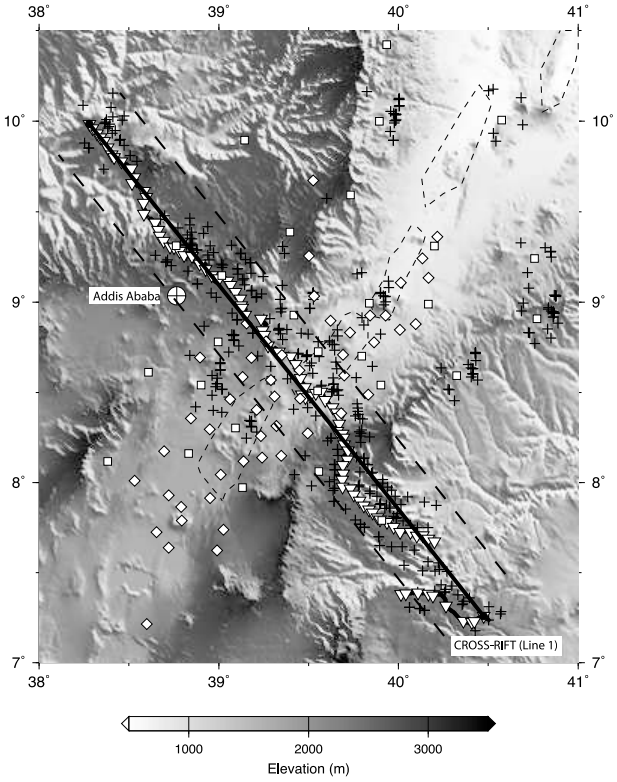


**Figure 3.** Location of EAGLE seismic stations. Phase I and phase II three-component broadband stations are marked by squares and diamonds, respectively. Phase III three-component broadband stations are marked by inverted triangles. The cross-rift best fit profile is shown with dashed lines marking 30 km distance from the profile. The surface projections of receiver function pierce points at 35 km depth are also shown with crosses. Zones of concentrated magmatism, or "magmatic segments," are shown by irregular dashed lines.

**Table 2.** Events Used for Phase III Receiver Function Analysis[a]

| Date and Time (UTM) | Latitude (deg) | Longitude (deg) | Depth (km) | Magnitude | Dist (deg) | Baz (deg) |
|---|---|---|---|---|---|---|
| 1 Dec 2002, 1437:23 | −11.24 | 117.26 | 19 | 5.6 | 81.3 | 103.0 |
| 2 Dec 2002, 0200:35 | −26.13 | 70.82 | 10 | 5.3 | 47.9 | 139.3 |
| 2 Dec 2002, 0458:55 | 37.75 | 21.09 | 10 | 5.6 | 31.7 | 333.5 |
| 2 Dec 2002, 1342:10 | 1.51 | 126.39 | 10 | 6.0 | 87.9 | 88.9 |
| 2 Dec 2002, 1821:50 | −6.52 | 71.43 | 10 | 4.9 | 36.9 | 115.1 |
| 4 Dec 2002, 1130:54 | 19.38 | 94.51 | 53 | 5.7 | 55.0 | 73.4 |
| 4 Dec 2002, 1550:42 | 38.73 | 142.19 | 40 | 5.0 | 94.5 | 49.6 |
| 14 Dec 2002, 1327:29 | 39.74 | 97.44 | 22 | 5.6 | 60.1 | 49.8 |
| 17 Dec 2002, 0432:53 | −56.95 | −24.83 | 10 | 6.3 | 84.3 | 209.4 |
| 18 Dec 2002, 1412:22 | −57.09 | −24.98 | 10 | 6.2 | 84.4 | 209.3 |
| 19 Dec 2002, 0342:46 | 0.91 | 126.27 | 33 | 5.6 | 87.9 | 89.5 |
| 21 Dec 2002, 1741:14 | 4.98 | 123.16 | 602 | 5.7 | 84.1 | 86.0 |
| 25 Dec 2002, 1257:06 | 39.57 | 75.22 | 29 | 5.7 | 44.1 | 41.9 |
| 25 Dec 2002, 1913:42 | 35.64 | 69.86 | 90 | 5.5 | 38.4 | 43.4 |
| 30 Dec 2002, 0449:09 | 7.47 | 123.41 | 10 | 6.3 | 84.0 | 83.5 |
| 6 Jan 2003, 1457:34 | 20.09 | 121.50 | 33 | 5.7 | 80.3 | 71.2 |
| 6 Jan 2003, 2343:51 | 15.65 | 119.66 | 10 | 6.0 | 79.1 | 75.9 |
| 9 Jan 2003, 0442:43 | 0.54 | 98.60 | 45 | 5.7 | 60.7 | 95.0 |
| 10 Jan 2003, 1525:59 | 0.22 | 97.92 | 26 | 5.3 | 60.1 | 95.5 |
| 14 Jan 2003, 1413:57 | 27.99 | 62.35 | 56 | 5.5 | 28.9 | 48.4 |

[a] Angular distances (Dist) and back azimuths (Baz) are calculated from the northwestern end of the EAGLE cross-rift profile. UTM, universal time meridian.

zero-phase Butterworth high-pass filter with a cutoff period of 10 s directly after calculation. Furthermore, applying a minimum-phase instead of a zero-phase high-pass filter to remove the long-period noise was explored to aid the identification of two phases at typical Moho conversion arrival times [*Cornwell*, 2008].

## 2.3. Binning and Stacking

[20] A form of migration was applied to each event-station pairing, where each RF is repositioned to the predicted location of the *P*-*S* conversion assuming an IASP91 Earth model [*Kennett and Engdahl*, 1991] with a Moho depth compatible with previous estimates (35 km). Figure 3 shows these predicted Moho piercing points projected vertically onto the surface for all the event-station pairs used to calculate RFs in this study. The individual migrated RFs were then stacked every 5 km along the best fit linear profile, using 30 $km^2$ bins (Figure 4).

## 2.4. Phase Identification

[21] To clarify the identification of phases on the observed RF profile, synthetic RFs were calculated at 5 km intervals from the coincident controlled source *P* wave velocity model (Figure 2) assuming a constant $V_p/V_s$ of 1.85, using the reflectivity method [*Kennett*, 1983] and the same processing parameters as those for the observed RFs (i.e., a Gaussian width of 1.0 or 2.0; a water level value of 0.001; and a fixed ray parameter of 0.06 s/km) (Figure 4a). The assumed $V_p/V_s$ value is expected to be a close first approximation for the crystalline crust, but is probably an underestimation for the low $V_p$ near-surface sedimentary layers [e.g., *Castagna et al.*, 1985].

### 2.4.1. Zero-Time *P* Phase

[22] The synthetic RF stacks show *P* arrivals at zero time, except between 150 and 240 km, where the *P* peaks are broadened and offset from zero by up to 0.4 s. This offset from zero time is indicative of the low-velocity sediments at the surface [e.g., *Cassidy*, 1992] modeled by *Mackenzie et al.* [2005]. The observed data show typical offsets of less than 0.2 s but more than 0.2 s between 130 and 240 km and the largest offset of nearly 0.4 s between 0 and 50 km along the profile. The offset *P* arrivals are modeled in section 3.1.

### 2.4.2. Phase $PpPs_{uc}$

[23] The phase $PpPs_{uc}$ has reflected as a *P* wave at the surface before being converted from the base of the sediments (i.e., the step from ~5 to >6 km/s at the top of the basement in the seismic velocity model, Figure 2). It occurs at times between 1.0 and 3.5 s after the *P* arrival in the synthetic RFs (Figure 4a) and is latest with the highest amplitudes beneath the rift valley. The phase $PpPs_{uc}$ typically occurs earlier in the observed RFs, at

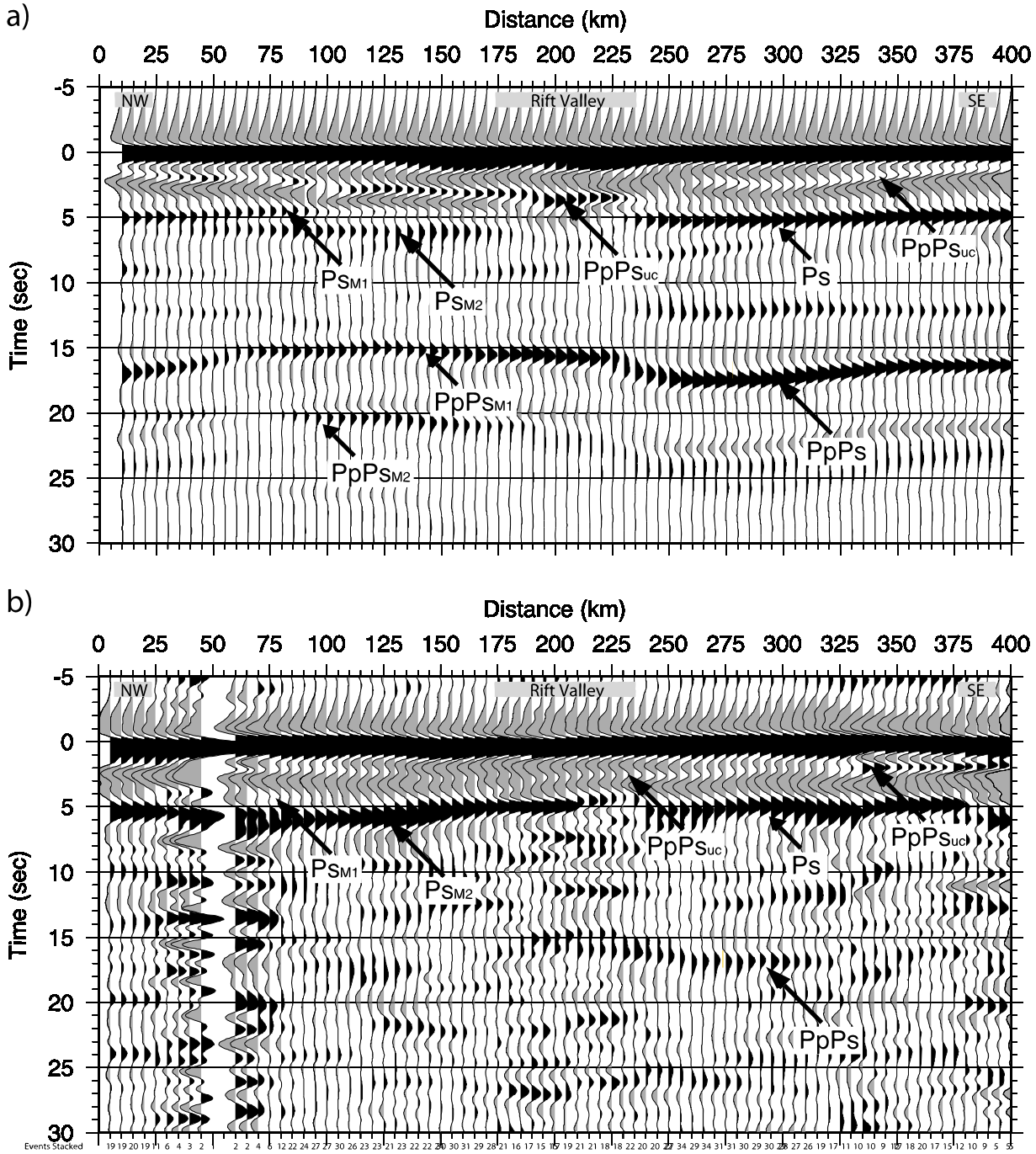


**Figure 4.** Cross-rift profile of binned and stacked (a) synthetic and (b) observed radial RFs after migration to their correct position at 35 km using the IASP91 Earth model [*Kennett and Engdahl*, 1991]. Note that the number of events stacked to make each bin trace is printed at the base of that trace. A Gaussian width of 2 was used to calculate the receiver functions (maximum frequency $\simeq$ 1.0 Hz), and a zero-phase high-pass filter (0.1 Hz) was applied to remove long-period noise. The synthetic receiver functions were calculated using the reflectivity method [*Kennett*, 1983] and the *P* wave velocity model shown in Figure 2 that was converted to both *S* wave velocity (using a constant $V_p/V_s$ of 1.85) and density (using the velocity-density relationship of *Cornwell et al.* [2006]).

1.5–2.5 s, with the largest amplitudes of this phase occurring in the southeasternmost 70 km of the profile. The arrival times of $PpPs_{uc}$ are used to constrain the depth to basement in section 3.2.

### 2.4.3. *Ps* Phase From the Moho

[24] The *P* to *S* wave conversion at the Moho is prominent at ~5 s at 0–25 km and 235–400 km

along the profile for both the synthetic and real RFs (Figure 4). The *Ps* peak is narrowest and occurs closer to ~4 s after the *P* arrival in northwestern parts the rift valley (175–205 km along the profile) and appears to be absent beneath the southeastern-most part of the rift valley. Within the rift *Ps* has reduced amplitudes, indicative of a smaller acoustic impedance contrast across the Moho or a gradational boundary. The reduced energy could also be caused by destructive interference with crustal reverberations, particularly if there is a sedimentary basin present close to the surface. This scenario seems unlikely, however, because the *P* and $PpPs_{uc}$ phases have similar arrival times across the entire rift, suggesting a consistent near-surface structure. Where identifiable, the *Ps* phase is used (with its multiples) to derive bulk crustal $V_p/V_s$ and thickness estimates in section 4.

#### 2.4.4. Phases $Ps_{M1}$ and $Ps_{M2}$

[25] The $Ps_{M1}$ and $Ps_{M2}$ are *P* to *S* conversions at the top and bottom, respectively, of the anomalously high $V_p$ (>7.2 km/s) lower crustal layer beneath the northwestern half of the profile (northwestern lower crustal layer (NWLCL)). In general, the synthetic RFs from the controlled source model show a small amplitude $Ps_{M1}$ phase at ~4.5 s and a marginally larger amplitude $Ps_{M2}$ phase at ~6 s, identifiable between 50 and 180 km along the profile (Figure 4a). For the observed RFs, the $Ps_{M1}$ phase occurs at ~4.0–4.5 s and typically has a small amplitude. It can be directly identified between 30 and 110 km along the profile and indirectly identified to 170 km as a broadened $Ps_{M2}$ phase peak. The $Ps_{M2}$ amplitudes are generally comparable to those of the Moho *Ps* phase to the southeast of the rift and the arrival times vary between ~5.0 and ~6.5 s. The timing and amplitude of these phases are modeled in section 3.3.

#### 2.4.5. Crustal Multiples

[26] There are strong reverberations from the Moho *Ps* phase reflected at the surface (*PpPs*) along the southeastern section of the profile at 15–18 s in the synthetic RFs. This phase is somewhat identifiable in the observed data, particularly between 235 and 320 km. The sharp discontinuities at the top and base of the lower crustal layer produce large-amplitude multiple energy between 15 and 21 s in the synthetic stacks, which is not observed in the real data. In the rift valley, the observed RFs display significant energy between 5 and 15 s, in addition to the multiple energy predicted by the synthetics at 15–17 s.

## 3. Forward Modeling

[27] Forward modeling was used to constrain the thickness, $V_p$ and $V_p/V_s$ of the near-surface sedimentary layer(s) and the high-$V_p$ lower crustal layer (NWLCL) that occurs beneath the northwestern half of the profile.

### 3.1. Sedimentary Thickness

[28] Picked *P* arrival maxima from stacks at 5 km intervals across the profile (Figure 5a) show offsets from zero time of 0.05–0.57 s with an estimated picking error of ±0.02 s. The presence of a low-velocity layer near the surface results in *P* arrivals offset from zero time because the resolution of the RFs is inadequate to separate the *P* arrival and base of the near-surface layer conversion peaks from each other [e.g., *Cassidy*, 1992]. The offset time is related to the frequency content of the RFs that sample the layer(s) and the thickness, $V_p/V_s$ ratio and *P* wave velocity ($V_p$) of the sedimentary layer and the $V_p/V_s$ ratio and $V_p$ of the layer below. The zero-time offsets are modeled assuming a simple two-layer model over a half-space with fixed parameters ($V_p$ = 5.0 km/s and $V_p/V_s$ = 1.75) determined from the controlled source model (Figure 2). Combinations of parameters within ranges of 0–2 km, $V_p/V_s$ = 2–4 and $V_p$ = 3–4 km/s were used to create the synthetic RFs which were matched with the observed offset times and waveforms. An example of a forward modeled synthetic RF compared with observed data is shown in Figure 5b.

[29] This forward modeling is nonunique, but indicates that models with sedimentary thicknesses between 0.5 and 1.0 km and realistic *P* wave velocities (3–4 km/s) and $V_p/V_s$ ratios (2–3) are acceptable. This layer extends ~50 km outside the confines of the rift valley, coincident with the extent of the lowest $V_p$ (<4 km/s) layer in the controlled source model (near to SP14 on Figure 2) and the synrift (Mio-Pliocene) rhyolites (Figure 1).

### 3.2. Depth to Basement

[30] Picked times of $PpPs_{uc}$ peaks (Figure 5c) increase toward the rift axis from both flanks, indicating that the depth to basement (where $V_p$ > 6 km/s) deepens into the rift, assuming that similar velocity characteristics exist above the boundary.

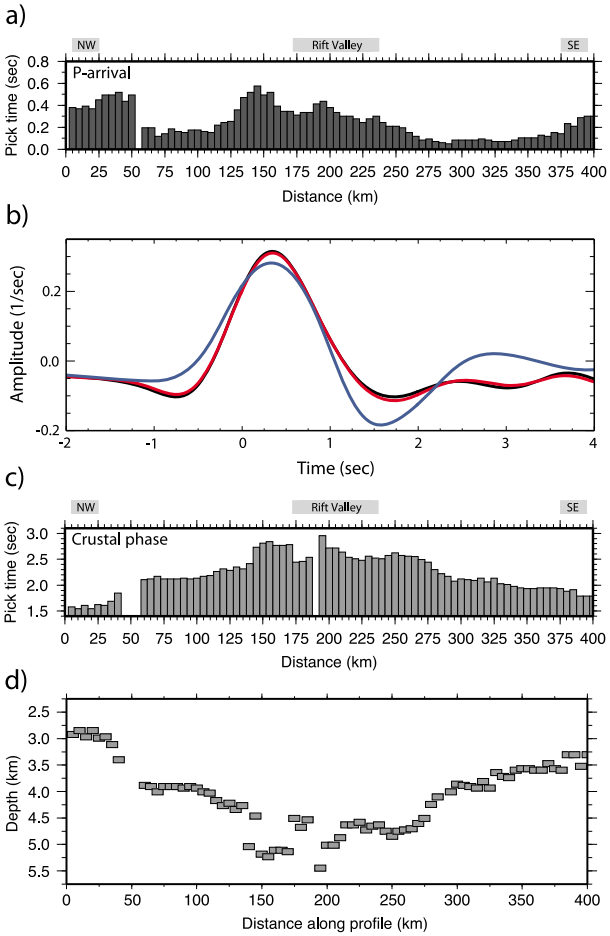


**Figure 5.** Analysis of $P$ and $PpPs_{uc}$ arrival times: (a) picked $P$ arrival times; (b) an example of comparing synthetic receiver functions (blue) with selected receiver function stacks (black indicates stack at 170 km; red indicates stack at 175 km along the profile) to model the $P$ arrival offsets; (c) $PpPs_{uc}$ phase picks; and (d) depth variation across the profile, calculated from the picked $PpPs_{uc}$ arrival times in Figure 5a using the equation given by *Zhu and Kanamori* [2000].

Using the formula that relates depth to a boundary with the $P$ to $PpPs$ time [*Zhu and Kanamori*, 2000], the picked times for this phase can be converted to depths (assuming a ray parameter of 0.06 s/km, $V_p$ = 5.0 km/s and $V_p/V_s$ = 1.75 above the boundary).

[31] The calculated depths to this discontinuity range between 2.8 and 6.0 km; the deepest are beneath the rift valley and shallowest at the far ends of the profile on the rift flanks (Figure 5d). The layer appears to thicken more gradually into the rift from the southeastern rift flank than from the northwestern flank where abrupt offsets in the discontinuity (with 0.5–0.8 km vertical change) occur near 50 km, 130 km and 260 km along the profile. The depth variation across the profile cannot be explained purely in terms of velocity changes as the physical properties of the layer would be geologically implausible (i.e., a 3 km depth change requires $V_p$ or $V_p/V_s$ changes of 2.5 km/s or 1.0, respectively). The presence of a varying near-surface low-velocity layer will change the average velocity of the upper layer in these synthetic tests, but this will only significantly change the depth estimates if the two layers are of similar thickness.

## 3.3. Northwestern Lower Crustal Layer

[32] The thickness of the NWLCL was initially determined from the difference in arrival time between the $Ps_{M1}$ and $Ps_{M2}$ peaks, where identifiable (Figure 4b), for a range of typical lower crustal $V_p/V_s$ values, following the method of *Zhu and Kanamori* [2000]. Following this analysis the waveforms of RF stacks are modeled to constrain the thickness, $V_p$ and $V_p/V_s$ of the NWLCL.

[33] During the arrival time analysis it is assumed that $Ps_{M1}$ and $Ps_{M2}$ originate from the top and base of the NWLCL and the average ray parameter is 0.06 s/km. The minimum-phase filtered RFs were employed in this analysis because they enable a double peak to be identified along a large proportion of the profile and the effect of filtering on the relative timing of the two peaks is minor [*Cornwell*, 2008]. Using the controlled source model (Figure 2), a constant $P$ wave velocity of 7.5 km/s is chosen for the NWLCL, whilst $V_p/V_s$ is varied between 1.75 and 1.95, since the calculated thickness ($h$) is less sensitive to variations in $V_p$ than $V_p/V_s$ [*Cornwell*, 2008]). Results show an overall thinning from 16 ± 2 km to 10 ± 1 km of the NWLCL toward the southeast, into the rift. This is opposite to that in the controlled source seismic model (Figure 2), where the lower crustal layer increases in thickness from approximately 10 to 16 km into the rift (toward the southeast). The NWLCL layer thickness is in the range 6.6–11.0 km in regions where a double peak is not clearly identified but can be estimated from a widened single peak (from 155 to 175 km along the profile, Table 3).

[34] Representative RF waveforms around 25 and 90 km on the profile (Figure 4b) were chosen for further modeling. Minimum-phase and zero-phase high-pass filters (0.1 Hz) were applied to both the stacked and synthetic RFs to aid the matching process. In line with the controlled source results, $V_p$ for this lower crustal layer was varied between 7.3 and 7.7 km/s whilst other layer parameters were kept constant (Table 4). The effects of varying

**Table 3.** Measured and Estimated Peak-to-Peak NWLCL Phase Times and Calculated Layer Thickness at Likely $V_p/V_s$ Ratios[a]

| Distance (km) | $\Delta t$ (s) | $h_{1.75}$ (km) | $h_{1.85}$ (km) | $h_{1.95}$ (km) | $h_{refr}$ (km) | $V_p$ (km/s) |
|---|---|---|---|---|---|---|
| 25 | **1.58** | 14.8 | 13.1 | 11.8 | *10.5* | *7.58* |
| 30 | **1.76** | 16.6 | 14.7 | 13.2 | *10.9* | *7.58* |
| 35 | **1.76** | 16.6 | 14.7 | 13.2 | *11.6* | *7.57* |
| 40 | **1.86** | 17.5 | 15.5 | 13.9 | *12.0* | *7.57* |
| 45 | **1.89** | 17.8 | 15.8 | 14.1 | *12.2* | *7.57* |
| 75 | **1.44** | 13.5 | 11.9 | 10.7 | *13.3* | *7.40* |
| 80 | **1.44** | 13.5 | 11.9 | 10.7 | *13.4* | *7.38* |
| 85 | **1.63** | 15.3 | 13.6 | 12.2 | *13.5* | *7.36* |
| 90 | **1.60** | 15.0 | 13.3 | 11.9 | *13.7* | *7.33* |
| 95 | **1.47** | 13.8 | 12.2 | 11.0 | *13.8* | *7.29* |
| 100 | **1.40** | 13.2 | 11.7 | 10.5 | *14.0* | *7.27* |
| 105 | **1.14** | 10.7 | 9.5 | 8.5 | *14.3* | *7.28* |
| 110 | **1.01** | 9.5 | 8.4 | 7.6 | *14.3* | *7.28* |
| 115 | 1.04 | 9.8 | 8.7 | 7.8 | *14.5* | *7.29* |
| 120 | 1.18 | 11.0 | 9.8 | 8.8 | *14.7* | *7.30* |
| 125 | 1.18 | 11.0 | 9.8 | 8.8 | *14.8* | *7.31* |
| 155 | 0.85 | 8.0 | 7.1 | 6.3 | *15.8* | *7.40* |
| 160 | 0.78 | 7.4 | 6.5 | 5.8 | *15.7* | *7.43* |
| 165 | 0.95 | 8.9 | 7.9 | 7.1 | *15.6* | *7.49* |
| 170 | 0.88 | 8.3 | 7.3 | 6.6 | *15.5* | *7.57* |
| 175 | 0.88 | 8.3 | 7.3 | 6.6 | *15.3* | *7.64* |

[a] Measured (bold) and estimated peak-to-peak NWLCL phase times ($\Delta t$) and calculated layer thickness for 30 km$^2$ bins at likely $V_p/V_s$ ratios (e.g., $h_{1.75}$). The seismic refraction model (Figure 2) high-$V_p$ lower crustal layer thickness ($h_{refr}$) and $V_p$ are shown in italics. All calculations follow *Zhu and Kanamori* [2000] and assume a constant $V_p$ of 7.5 km/s and $p$ of 0.06 s/km.

NWLCL thickness, $P$ wave velocity and $V_p/V_s$ on the arrival times and amplitudes of $Ps_{M1}$ and $Ps_{M2}$ were investigated by *Cornwell* [2008], with the best fitting models presented in this paper.

[35] The observed RF stack at 25 km along the profile shows $Ps_{M1}$ and $Ps_{M2}$ with similar amplitudes when minimum-phase filtered (Figure 6a). The best fit model of the NWLCL has a $V_p$ of 7.5 km/s, $V_s$ of 3.90 km/s ($V_p/V_s$ of 1.93) and a thickness of 10 km, with a top boundary at a depth of 32 km.

[36] The observed RF stack at 90 km is representative of those from 80–105 km along the cross-rift profile, with a lower-amplitude $Ps_{M1}$ than $Ps_{M2}$ (Figure 6b). As there is a five-fold increase in the summed RFs, the quality of these stacks is higher than at 25 km. There is little evidence in the waveforms of multiple phases from this layer, which is indicative of either small or gradational boundaries at the top and base of the NWLCL, or a reduction of multiple phase energy due to destructive interference with other phases. Assuming a

**Table 4.** Starting Model Parameters for NWLCL Forward Modeling

| Layer | $V_p$ (km/s) | $V_s$ (km/s) | Density (kg/m$^3$) | Thickness (km) |
|---|---|---|---|---|
| 1 | 5.00 | 2.86 | 2590 | 4 |
| 2 | 6.30 | 3.60 | 2840 | 26 |
| 3 | 7.50 | 4.29 | 3150 | 13 |
| 4 | 8.10 | 4.63 | 3330 | $\infty$ |

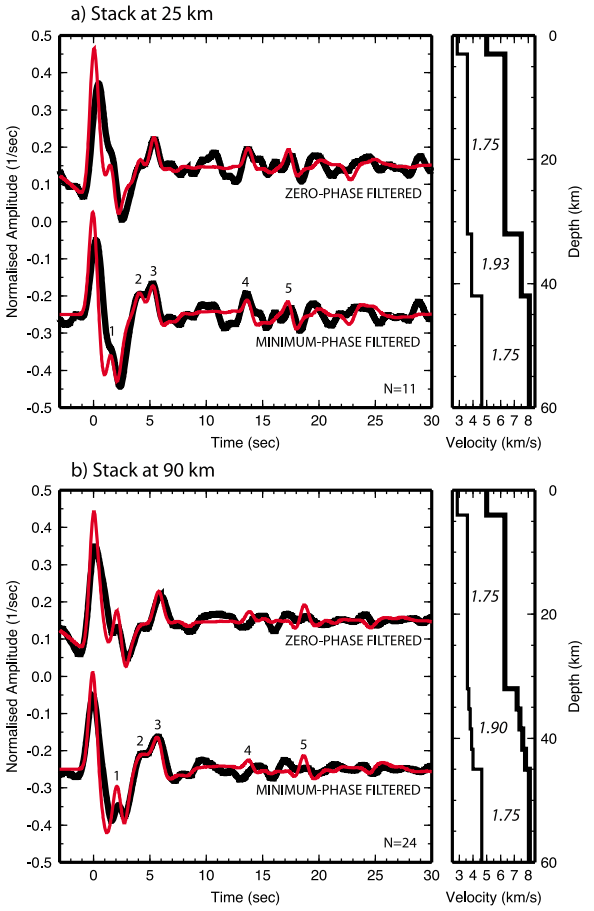


**Figure 6.** A comparison of stacked filtered real and synthetic radial receiver functions at (a) 25 and (b) 90 km along the profile. Velocity model containing a simple northwestern lower crustal layer (NWLCL) as shown (Figure 6a) (NWLCL model parameters are $V_p$ = 7.50 km/s, $V_s$ = 3.90 km/s, $V_p/V_s$ = 1.93, $h$ = 10 km, and $D_{M1}$ = 32 km; $V_p/V_s$ = 1.75 elsewhere in the model) and a gradational northwestern lower crustal layer (Figure 6b) (NWLCL model parameters are $V_p$ = 7.20–7.80 km/s, $V_s$ = 3.69–4.00 km/s, $V_p/V_s$ = 1.90, $h$ = 13 km, and $D_{M1}$ = 32 km; $V_p/V_s$ = 1.75 elsewhere in both models). The conversions and multiple phases $PpPs_{uc}$ (indicated by 1), $Ps_{M1}$ (indicated by 2), $Ps_{M2}$ (indicated by 3), $PpPs_{M1}$ (indicated by 4), and $PpPs_{M2}$ (indicated by 5) are also labeled. Receiver functions are as follows: bold black indicates observed, and thin red indicates synthetic. Velocity model lines are as follows: bold indicates $V_p$, and thin indicates $V_s$.

discontinuity at the layer boundaries, the best fitting model at 90 km has a $V_p$ of 7.5 km/s, $V_s$ of 3.75 km/s ($V_p/V_s$ of 2.00), a thickness of 11.5 km and a top boundary at a depth of 33.5 km.

[37] A gradational upper NWLCL boundary, however, is considered to best match the observed waveforms of $Ps_{M1}$ and $Ps_{M2}$. Various velocity gradients were tried, which have the effect of reducing the amplitude of $Ps_{M1}$ (and $PpPs_{M1}$), with gradients occurring over larger vertical distances showing the greatest amplitude reduction. A gradual increase in $V_s$ on the top boundary from 3.69 to 4.00 km/s over 13 km produces a good fit to the observed waveforms (Figure 6b). The gradient is actually modeled as stepwise linear increase in $V_p$ and $V_s$ (NWLCL parameters are: $V_p$ = 7.20–7.80 km/s; $V_s$ = 3.69–4.00 km/s; $V_p/V_s$ = 1.90; $h$ = 13 km; $D_{M1}$ = 32 km). Even if the whole of the NWLCL is characterized by a velocity gradient, a double peak (i.e., $Ps_{M1}$ and $Ps_{M2}$) still appears in the resulting synthetic RF. To obtain an optimum waveform fit, the $V_p/V_s$ in the layer has to be reduced slightly to 1.90. *Cornwell* [2008] found that a layer with gradational properties can produce similar relative $Ps_{M1}$ and $Ps_{M2}$ amplitudes as raising the $V_p/V_s$ in a layer with discontinuities as boundaries.

## 4. Crustal Thickness and $V_p/V_s$: $H$-$\kappa$ Stacking

### 4.1. Overview

[38] The $H$-$\kappa$ stacking method of *Zhu and Kanamori* [2000] was applied to the observed cross-profile RF stacks (Figure 4b) to produce estimates of crustal thickness ($H$) and average crustal $V_p/V_s$ ($\kappa$). This technique stacks the amplitudes of RFs at the predicted arrival times of *Ps*, *PpPs* and *PpSs* + *PsPs* for various values of $H$ and $V_p/V_s$. It is assumed that there is a clear Moho *Ps* phase as well as crustal multiples *PpPs* and *PpSs* + *PsPs*. An average *P* wave velocity for the crust of 6.25 km/s was applied to all stacking calculations, close to the average crustal $V_p$ values from the controlled source model and the mean of the average crustal $V_p$ values for previous RF $H$-$\kappa$ studies in Ethiopia (Table 1).

### 4.2. $H$-$\kappa$ Analysis in the Presence of an Anomalous ($V_p$ > 7.2 km/s) Lower Crustal Layer

[39] Where a high-$V_p$ (>7.2 km/s) lower crustal layer exists, the $H$-$\kappa$ stacking method may be used to find either (1) the average crustal $V_p/V_s$ and crustal thickness above or (2) the average crustal $V_p/V_s$ and crustal thickness including the layer. In addition to a double *Ps* phase, the presence of a high-$V_p$ lower crustal layer will create two *PpPs* and *PsPs* + *PpSs* phases that may constructively stack to produce false maxima in $H$-$\kappa$ space.

[40] An $H$-$\kappa$ estimate should therefore be considered reliable only if the maximum $H$-$\kappa$ stack amplitude is found from the (weighted) sum of phase amplitudes from the same horizon (e.g., *Ps*, *PpPs* and *PsPs* + *PpSs* associated with the top of an identified lower crustal layer). Reliable $H$-$\kappa$ estimates in the presence of a lower crustal layer, therefore, require that (1) the observed reverberations are correctly identified as originating from either the top or base of the layer and (2) combinations of phases from the same boundary are used. Furthermore, RFs without sufficient bandwidth to create separate peaks indicative of a lower crustal layer may produce unreliable $H$-$\kappa$ stacking results. We investigate this effect by performing $H$-$\kappa$ analysis on cross-rift profile stacked RFs that were calculated with both a maximum frequency of ~0.5 and ~1.0 Hz.

### 4.3. Results

[41] Reliable estimates of bulk crustal thickness ($H$) and $V_p/V_s$ (Figure 7) were achieved primarily beneath the rift valley and southeastern rift flank, where results from lower- and higher-frequency stacks in the same location were within calculated error bars in most cases (Figure 8). Based upon the obtained values of $H$ and $V_p/V_s$, the profile can be divided into four distinct regions: (1) beneath the northwestern rift flank (from 25 to 160 km along the profile) with $V_p/V_s$ likely to be in the range 1.80–1.88 (but possibly as high as 2.00) and $H$ likely to be 34–41 km (but possibly as deep as 48 km) with evidence for a lower crustal layer, (2) beneath the rift valley (from 160 to 245 km) where $V_p/V_s$ = 1.84–1.92 and $H$ = 33–36 km, (3) beneath the southeastern rift flank (from 275 to 375 km) where $V_p/V_s$ = 1.78–1.85 and $H$ = 37–40 km, and (4) a transition zone between the rift valley and southeastern rift flank zones (from 245 to 270 km) where $H$ increases from ~35 km to ~40 km and $V_p/V_s$ decreases from ~1.92 to ~1.76 (Figure 8).

[42] At the far northwestern end of the profile, both the low- and high-frequency results estimate an $H$ value of ~48 km with a corresponding $V_p/V_s$ of ~1.68. Estimates for the neighboring stacks at 25 and 30 km are significantly different with an

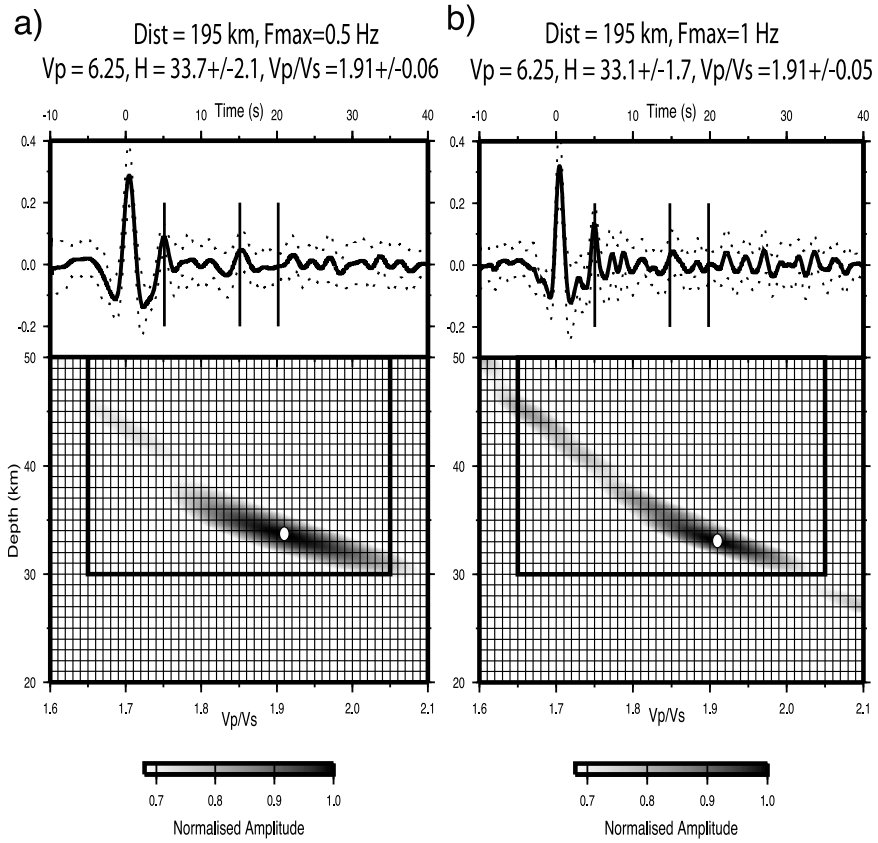


**Figure 7.** An example of a (a) low-frequency and (b) high-frequency $H$-$\kappa$ result for a single stack at 195 km (note that the low- and high-frequency results also depict an example of a quality of 1 = good and 2 = fair, respectively).

$H$ of ~39 km and $V_p/V_s$ of ~1.84. Beneath the remainder of the northwestern rift flank where the NWLCL has been estimated to be up to 18 km thick, reliable results were only obtained with stacks with the lower frequencies. $V_p/V_s$ estimates here are in the range 1.82–1.84 and crustal thickness 40–42 km (Figure 8). The high-frequency $H$ and $V_p/V_s$ estimates rise sharply, perhaps providing indirect evidence the presence of a NWLCL that is sufficiently thick to affect the $H$-$\kappa$ technique results.

[43] Beneath the northwestern part of the rift valley, $H$ is estimated to be in the range 32–34 km with $V_p/V_s$ between 1.90 and 1.91. It is difficult to obtain $H$-$\kappa$ results beneath the southeastern part of the rift valley because the phase from the Moho is either absent or has a low amplitude.

## 5. Interpretation and Discussion

### 5.1. Near-Surface Layers and Basement Structure

[44] The uppermost low-velocity ($V_p$ = 3–4 km/s; $V_p/V_s$ = 2–3) layer that occurs beneath and to the northwest of the rift valley was defined by forward modeling to be less than 1 km thick and correlates with the extent of a low-velocity ($V_p \approx$ 3.3 km/s) and low-density (~2380 kg/m$^3$) layer modeled using seismic refraction/wide-angle reflection [*Mackenzie et al.*, 2005] and high-resolution gravity data [*Cornwell et al.*, 2006]. This layer corresponds to the northwestern rift margin region and the rift valley, where Miocene–Early Pliocene age pyroclastic and basaltic rocks and Plio-Holocene fluvio-lacustrine sediments crop out on the surface [e.g., *Kazmin*, 1975; *Wolfenden et al.*, 2004; *Abebe et al.*, 2005] (Figures 1 and 9).

[45] Stratigraphically below the Miocene pyroclastic rocks is over 3 km of Jurassic-Paleogene marine sediments and the Oligocene flood basalt series [*Tefera et al.*, 1996] (Figure 1). The upper crustal basement discontinuity forms the base of these sediments and is deepest beneath the rift valley (~6.0 km) and shallowest (~2.8 km) at the ends of the profile. Interpreted as the top surface of the Precambrian basement, this interface corresponds to an increase in $P$ wave velocity of more than

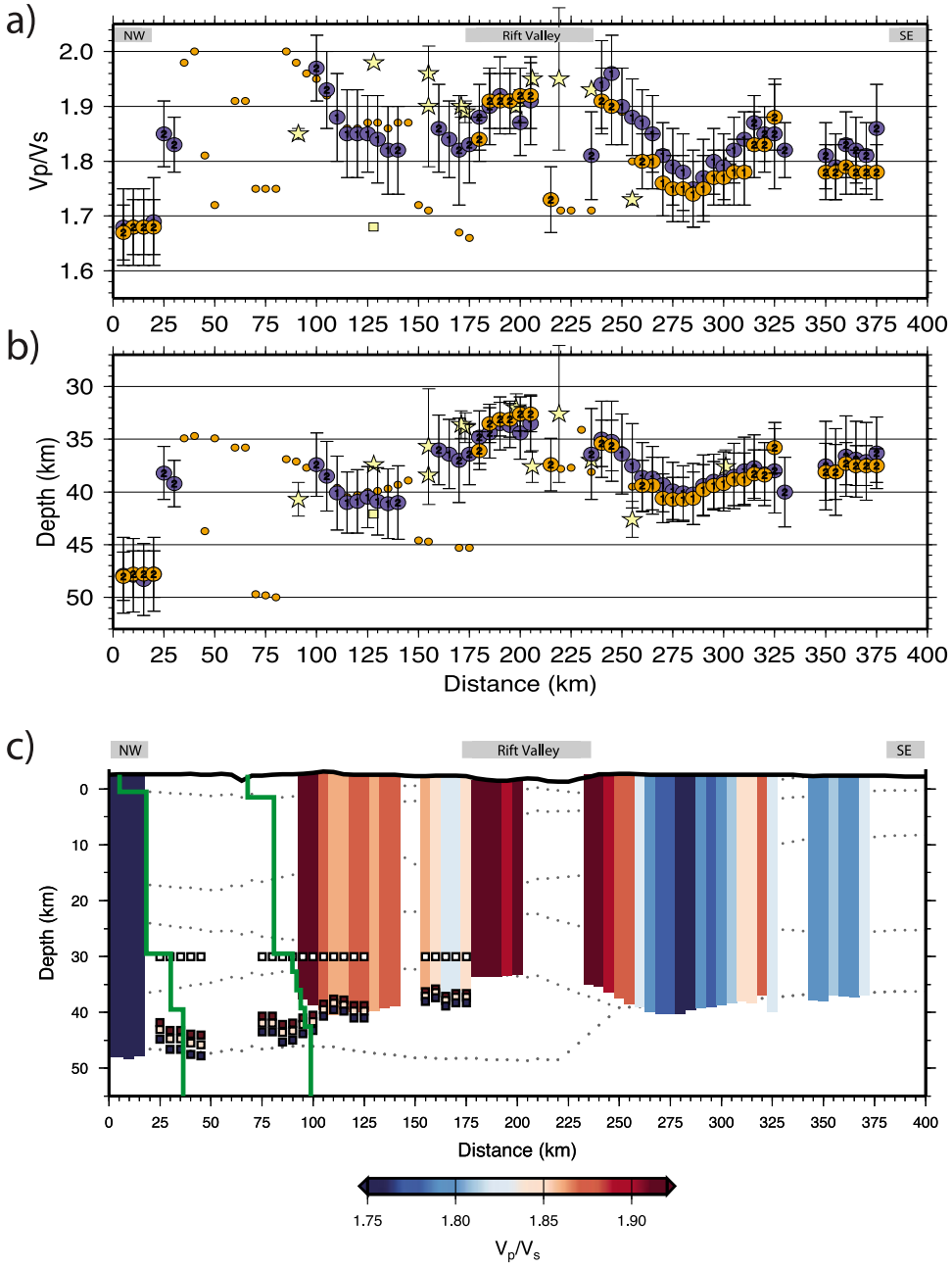


**Figure 8.** Cross-rift profile $H$-$\kappa$ stacking results, shown as (a) $V_p/V_s$ ($\kappa$) and (b) crustal thickness ($H$) (labeled as depth). Large blue and orange circles denote the low-frequency (<0.5 Hz) and high-frequency (<1 Hz) results, respectively, with 1 = good and 2 = fair quality. Small orange circles show high-frequency results probably influenced by the presence of a high-$V_p$ lower crustal layer. Nearby $H$-$\kappa$ stacking results by *Stuart et al.* [2006] and *Dugda et al.* [2005] are projected onto the line and shown as yellow stars and squares, respectively. (c) Summary diagram showing the NWLCL best fit forward models at 25 km and 90 km (Figure 6) in green, thickness estimates from peak-to-peak times (Table 3) with filled squares according to layer $V_p/V_s$ (upper boundary is fixed at 30 km), and $H$-$\kappa$ stacking results as colored bars. Background grey dots depict the major horizons imaged by the seismic model in Figure 2.

1 km/s [*Mackenzie et al.*, 2005] (Figure 2). Major offsets in the basement are imaged at 50, 140 and 275 km along the profile (Figure 5d). These structures coincide with the surface locations of large-offset rift border fault zones (Figure 9) and are interpreted to be related to the early mechanical stretching phase of rift evolution. Their location, in addition to the extent of the uppermost sediments, suggests that early rift-related extension appears to be confined to a ~100 km wide zone; the present-

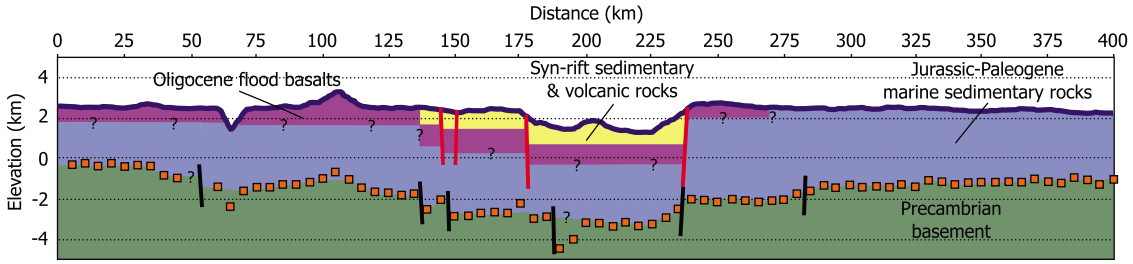


**Figure 9.** Sketch diagram of the likely near-surface structure and simplified geological units beneath the cross-rift profile, derived from analysis of receiver functions. Calculated depths to basement (orange squares) are plotted, with the size of the squares representative of the depth range beneath each station (assuming an upper layer where $V_p$ = 4.8–5.2 km/s and $V_p/V_s$ = 1.70–1.85). Bold black lines mark the locations of steps in the modeled boundary. Red lines mark prominent fault zones identified by *Wolfenden et al.* [2004]. The profile is oriented NW (0 km) to SE (400 km) with a vertical exaggeration of 10:1.

day rift valley occupies the southeasternmost 60 km of this zone (Figures 1 and 9). Since the Jurassic-Paleogene sedimentary sequence is observed to rest unconformably on Precambrian basement [*Dow et al.*, 1971; *Garland*, 1972], these basement faults may be evidence of a predepositional basement topography.

[46] The lower boundary of the Oligocene flood basalt sequence is not well resolved by this study, but it can be observed in the field at both rift margins [*Wolfenden et al.*, 2004] and it occurs in the Mugher Gorge (located at ~70 km along the profile, see Figure 9). The floor of the gorge is composed of marine sediments, thus indicating the thickness of the flood basalts to a be <800 m in this region.

## 5.2. Crust Beneath the Northern Main Ethiopian Rift

[47] The *H*-$\kappa$ technique provides estimates of an average crustal $V_p/V_s$ and a crustal thickness. $V_p/V_s$ values can be directly converted into Poisson's ratios ($\sigma$), which are commonly used to characterize bulk crustal composition. The high bulk crustal $V_p/V_s$ (1.84–1.92) beneath the rift valley section of the profile suggests that the crust is either composed predominantly of mafic material [*Christensen*, 1996] and/or contains a significant volume of partial melt [*Watanabe*, 1993; *Owens and Zandt*, 1997]. Within the center of the rift, beneath the Boset magmatic segment (Figure 1), a 20 km wide zone of elevated upper crustal *P* wave velocity and density has been interpreted as mafic (gabbroic) intrusions into the upper (and possibly lower) crust, associated with focussed Quaternary-Recent magmatism [*Mahatsente et al.*, 1999; *Keranen et al.*, 2004; *Mackenzie et al.*, 2005; *Cornwell et al.*, 2006]. The results obtained in this study agree with the anomalously high $V_p/V_s$ values of up to 2.08 identified beneath the NMER and Afar by previous RF studies (Table 1) in the rift [*Ayele et al.*, 2004; *Dugda et al.*, 2005; *Stuart et al.*, 2006]. The present study, however, provides higher spatial sampling needed to image rift structure and magmatic modification of the crust. The local earthquake study of *Daly et al.* [2008] shows $V_p/V_s$ values of 1.81–1.84 beneath the rift axis between 12 and 25 km depth, which they interpret as cooled mafic dikes.

[48] The highest estimates of average $V_p/V_s$ occur in the thinnest crust (~32 km) beneath the northwestern side of the rift valley. Major element mass balance and thermodynamic modeling of geochemical data suggest that the lavas erupted in this (northwestern) part of the rift during the Quaternary fractionated at various levels between the base of the crust and the near-surface [*Rooney et al.*, 2007]. Gravity modeling requires a ~12 km wide zone containing considerable (at least 40%) frozen mafic magma at depths greater than 10 km beneath this region [*Cornwell et al.*, 2006], upper and middle crustal tomography shows $V_p/V_s$ values of up to 1.85 [*Daly et al.*, 2008] and *Whaler and Hautot* [2006] interpret a conductive lower crust as evidence of partial melt. Deep seismicity (>25 km) in this region has been attributed to ongoing magma injection into the lower and middle crust by *Keir et al.* [2009].

[49] An absence of *Ps* energy converted at the Moho is observed beneath the southeastern half of the rift valley (e.g., Figure 4b). The cause of this "Moho hole" could be (1) destructive interference of Moho conversions with crustal converted phases and their reverberations, (2) an *S* wave velocity gradient (rather than a typical sharp Moho contrast) at the base of the lower crust, (3) low *S* wave velocity in the uppermost mantle that significantly

reduces the shear wave velocity contrast [*Zandt et al.*, 2004], and (4) anisotropy at or near the Moho resulting in *P-SH* converted energy (rather than the *P-SV* energy shown in Figure 4b) [e.g., *Levin and Park*, 1997]. Since crustal phases (e.g., $PpPs_{uc}$) are coherent across the entire rift valley and do not interfere with the Moho conversions explanation 1 is unlikely (Figure 4b). There is evidence for anisotropy at predicted Moho depths in the form of coherent *P-SH* converted energy ~4 s after the *P* arrival [*Cornwell*, 2008], but the resolution of the RFs has so far precluded this from being modeled. The waveforms of the RFs do not provide enough information to discriminate between models of low-velocity uppermost mantle or a gradational Moho. Both models imply the presence of magmatism near the base of the crust beneath this part of the rift valley; the extent of the "Moho hole" delineates the 20–25 km wide zone of magma-derived new crust within the rift valley. *Mackenzie et al.* [2005] observed high-amplitude and high-frequency reflected Moho phases within this part of the rift valley and interpreted these as lower crustal sills. Geochemical evidence has been interpreted to suggest that magmas in this (southeastern) part of the rift have risen quickly from lithospheric mantle depths (~53–88 km) to within ~5 km of the surface before undergoing significant fractionation to produce large Quaternary felsic volcanoes [*Rooney et al.*, 2005, 2007]. In the same region within the crust, *Whaler and Hautot* [2006] imaged an electrically conductive zone between 15–25 km depth which they interpreted to contain partial melt and *Cornwell et al.* [2006] defined a 20 km wide zone of inferred gabbroic intrusions at a depth of about 8 km from gravity interpretation.

## 5.3. Ethiopian Plateau Crust: NW Part of the Profile

[50] The most reliable estimates (from low-frequency RFs) indicate that the NW rift margin and rift flank crust is thicker (36–42 km) and less mafic ($V_p/V_s$ = 1.80–1.88) than that beneath the rift valley. This is supported by both *Dugda et al.* [2005] and *Stuart et al.* [2006], who find crust with a thickness and $V_p/V_s$ of 38–44 km and 1.80–1.82 in this region of the western Ethiopian plateau (but do not take account of a high-$V_p$ lower crustal layer). Tomography in the uppermost ~20 km of the crust indicates $V_p/V_s$ values of 1.72–1.76 beneath the NW plateau [*Daly et al.*, 2008] and *Whaler and Hautot* [2006] show a 10–15 km thick resistive upper crust above a more conductive lower crust beneath the northwestern rift flank, compared to a <5 km thick resistive layer beneath the rift valley. These observations probably signify that a mafic lower and middle crust is overlain by a more felsic upper crust, which, when sampled together, produce the observed high bulk crustal $V_p/V_s$ estimates beneath the NW plateau and rift margin, but not as high as the mainly mafic crust beneath the NMER (Figure 8c).

### 5.3.1. Extent of the NWLCL

[51] Forward modeled depths to the upper boundary of the NWLCL of 29–31 km are consistent, within error, with depths determined by seismic refraction/wide-angle reflection by *Mackenzie et al.* [2005] for all but the northwestern end of the profile. This upper interface could be gradational, particularly where the layer is thinnest, with the sharpest changes in $V_p$ modeled to occur where the NWLCL is thickest. We interpret this boundary to mark the upper limit of mafic intrusive material into the lower crust. In a similar study, *Harland et al.* [2009] modeled a 6 km thick high-velocity (>7.0 km/s) lower crust beneath the Faroe Islands to have a gradational upper boundary and, following arguments by *White et al.* [2008], interpret the layer as heavily intruded crust, rather than "underplated" igneous rock.

[52] Depths to the base of the NWLCL of 41–42 km (using single RF stacks) and 36–46 km (from double-peak times) are shallower than in the controlled source model (49–50 km), but a good resolution was achieved for only ~60 km of this boundary (Figure 2). Forward modeling constrains the thickness of the NWLCL to between 6 and 18 km (assuming constant layer $V_p$ and $V_p/V_s$ values of 7.3–7.7 km/s and 1.75–1.95, respectively), with the thinnest parts of the NWLCL occurring beneath the northwestern rift margin, unlike the refraction/wide-angle reflection results that imply a thickening of the NWLCL toward the NMER [*Mackenzie et al.*, 2005] (Figure 8c).

[53] The high $V_p/V_s$ (>1.85) of the NWLCL produces an upper boundary with a large $V_p$ and small $V_s$ discontinuity, whereas the lower boundary displays a relatively small $V_p$ and a large $V_s$ discontinuity (if a general increase in $V_p$ with depth is assumed) (e.g., Figure 6a). The refraction/wide angle reflection method is sensitive to changes in $V_p$ and preferentially images the upper boundary, whereas RFs preferentially image the lower boundary (Figure 4). This may explain the discrepancy between the two methods when constraining the geometry of the NWLCL and in other regions

worldwide where a similar layer is imaged [e.g., *Tomlinson et al.*, 2006].

### 5.3.2. Composition, Internal Structure, and Source of the NWLCL

[54] The $V_p/V_s$ values of 1.85–1.93 indicate that the layer is composed mainly of mafic material and/or a small percentage of partial melt is present [e.g., *Watanabe*, 1993; *Owens and Zandt*, 1997]. A 50 km deep layer consisting entirely of frozen gabbro at moderate to high temperatures would produce a $V_p/V_s$ of ~1.87 and $P$ wave velocities similar to the 7.0–7.4 km/s obtained from well-resolved regions of the seismic refraction/wide-angle reflection model [*Christensen*, 1996; *Mackenzie et al.*, 2005]. However, layering within the NWLCL is inferred by the high-amplitude and high-frequency reverberatory signature [*Mackenzie et al.*, 2005; *Maguire et al.*, 2006]. A similar reflective character within the lower crust beneath Kenya was modeled as either igneous intrusions (sills) or magma chamber cumulates [*Birt*, 1996; *Thybo et al.*, 2000]. It is difficult to determine the proportion of intruded gabbroic sills compared to metamorphosed lower crust because the measured and modeled seismic velocities of gabbro ($V_p$ = 7.3 km/s; $V_s$ = 4.0 km/s; $V_p/V_s$ = 1.83) are very similar to those of some metamorphosed lower crustal rocks (e.g., the granulite facies of metabasic rocks) [*Christensen and Mooney*, 1995].

[55] The thickest parts of the NWLCL are situated directly above parts of the Ethiopian hot spot, a 500 km wide low $P$ and $S$ wave velocity zone at depths of 75 to 400 km in the upper mantle, which extends westward outside the confines of the rift valley [*Bastow et al.*, 2005; *Benoit et al.*, 2006a, 2006b; *Bastow et al.*, 2008], elucidating the likeliest source for the magmatic addition. If these features are linked, a predominantly vertical ascent of magma through the mantle is inferred, although we expect that significant lateral movement of magmas has also occurred during the long magmatic history of the region.

### 5.3.3. Emplacement of the NWLCL and Melting of the Lower Crust

[56] If the NWLCL is assumed to be composed of 100% gabbro and laterally continuous with an average thickness of 10 km beneath the entire Ethiopian plateau (a surface area of more than 800,000 km$^2$), the required volume of emplaced gabbro is roughly 8,000,000 km$^3$. Emplacement would have taken place either within the estimated 1 Myr of high-magma flux that produced the major flood basalt sequences [*Hofmann et al.*, 1997; *Rochette et al.*, 1998; *Coulie et al.*, 2003] or over a longer time period that is more consistent with the episodic (possibly minor) basaltic volcanism [*Chernet et al.*, 1998] and/or major uplift that began at 29–25 Ma [*Pik et al.*, 1999; *Gani et al.*, 2007]. This postulated amount of emplaced gabbro appears disproportionately high compared with the estimated flood basalt volume of ~180,000 km$^3$ [*Kieffer et al.*, 2004] and implies that only a small fraction of the mafic material reached the surface (this is the case even if the NWLCL is a local feature).

[57] Following work by *White et al.* [2008], adding a 15 km layer of magmatic intrusive material with a $P$ wave velocity of 7.3 km/s requires a positive mantle temperature anomaly of 150–175 K, assuming instantaneous emplacement. If this hot material is emplaced into the lower crust it would raise the regional geotherm and partially melt portions of it, potentially creating a layer of silicic magmas above the NWLCL [*Huppert and Sparks*, 1988; *Bergantz*, 1989; *Whittington et al.*, 2009]. *Annen and Sparks* [2002] modeled repeated basalt sill intrusion into the lower crust and found that the main controls on the generation of melt are (1) the rate of magma intrusion, (2) the composition and water content of the preexisting crustal rocks, and (3) the temperature and water content of the intruding basalt magma. Melt generation involves simultaneous cooling and crystallization of intruding magma and partial melting of both new mafic crust and the preexisting old crust. The proportion of these components depends on the fertility of the crust and the temperature and water content of the mafic magma. Fractional crystallization of the NWLCL is therefore a strong candidate as the source of the rhyolitic ignimbrites that contribute 20% of the volume of Ethiopian flood basalt province rocks [*Ayalew et al.*, 2002]. Where it extends beneath the rift, the NWLCL could therefore provide the geochemically derived enriched mantle source with an lower crustal component proposed by *Furman et al.* [2006].

### 5.3.4. Effects of the NWLCL on Rift Initiation and Evolution

[58] The new results imply that rifting is located where the least amount of magma has been emplaced into the lower crust. Whilst magmatic emplacement may have strengthened the crust by thickening it and increasing its component of relatively strong olivine rheology, the lithosphere

will be locally weakened, because the quartzofeldspathic rheology of the crust is weaker than the olivine rheology of the mantle [*Kusznir and Park*, 1987]. As such, the NWLCL would have played an important role in defining where strain was accommodated during rift initiation, assuming that a significant proportion of it had already been emplaced. It also appears to have had a role in the more recent strain-focusing stage of NMER evolution, since the current narrow rift was formed where the NWLCL is thinnest or absent. Furthermore, crystallized magma intruded into the lower crust may inhibit the later injection of dikes, as high-density upper crustal dikes are only modeled in regions beneath the southeastern sector of the rift [*Cornwell et al.*, 2006], forming a well-developed magma system where no NWLCL has been imaged [*Rooney et al.*, 2007].

### 5.4. Somalian Plate Crust: SE Part of the Profile

[59] The estimated average crustal $V_p/V_s$ of 1.74–1.82 of the Somalian Plate indicate a felsic-intermediate crust underlies the majority of the southeastern rift flank (Figure 8c). A highly resistive upper and lower crust beneath the southeastern rift flank (markedly different to the resistive upper and conductive lower crust beneath the northwestern rift flank) is constrained by magnetotelluric (MT) work [*Whaler and Hautot*, 2006] but similar crustal *P* wave velocity (apart from the addition of the high-$V_p$ lower crustal layer) are imaged by the coincident refraction/wide-angle reflection model. There is no geophysical or geochemical evidence of extensive magmatism beneath the parts of the southeastern rift flank sampled in this study. The crustal thickness of the Somalian Plate crust ranges from 37 to 41 km using the *H*-$\kappa$ stacking method, similar to that found by *Stuart et al.* [2006] (38–40 km) and *Dugda et al.* [2005] (37–42 km). *Mackenzie et al.* [2005] modeled a Moho depth of 39–40 km (i.e., 35 km of crystalline crust overlain by 4–5 km of sediments) from seismic refraction/wide angle reflection data along the same profile and *Tiberi et al.* [2005] estimated a crustal thickness of ~40 km using gravity and topography data.

[60] A ~35 km wide region corresponding to the southeastern rift margin is interpreted as the transition zone between magmatic and amagmatic crust, with average crustal $V_p/V_s$ decreasing from ~1.92 to ~1.76. Crustal thinning of ~5 km is estimated within this transitional zone, identical to that modeled by *Mackenzie et al.* [2005]. The synrift sedimentary rocks do not cross this transition and the large-offset Arboye border fault is also coincident with the northwestern limit of the transition zone [*Wolfenden et al.*, 2004]. The transition zone was therefore likely to be present in the earliest stage of rifting, which probably formed a ~100 km wide extensional half graben that developed to become the more focussed to the narrow ~60 km of the present day. It is likely that a preexisting terrane boundary, suture or shear zone [e.g., *Berhe*, 1990; *Stern*, 1994; *Abdelsalam and Stern*, 1996; *Yihunnie and Tesfaye*, 2002; *Johnson and Woldehaimanot*, 2003], which may produce a locally weak zone or an adjacent locally strong zone, has been exploited by the early extension and later magmatism in this location, which had a strong influence on rift evolution from its inception.

## 6. Conclusions

[61] 1. A <1 km thick layer consisting of low-velocity synrift (Miocene-Recent) deposits extends beneath and up to 50 km to the northwest of the present-day rift valley floor, marking the ~110 km wide region over which strain was accommodated during the early stages of rifting.

[62] 2. A layer consisting of Jurassic-Paleogene marine sedimentary rocks occurs over the entire length of the profile (400 km) with likely *P* and *S* wave velocities of 3.4–4.4 and 2.0–2.5 km/s. The unit marks the last period that the uplifted Ethiopian plateau was at sea level, has a thickness of more than 3 km and thickens from the northwest to the southeast.

[63] 3. A 2.8–6.0 km deep unconformity between Jurassic marine sedimentary rocks and Precambrian crystalline basement rocks is deepest beneath the rift valley and shallowest at the ends of the profile. Some large (<1 km) offsets in basement topography are correlated with major rift faults within the wide strained region, whereas others occur beneath both rift flanks.

[64] 4. There are major variations in crustal thickness and seismic properties along the NW–SE cross-rift profile that divide the crust into four regions: (1) ~115 km of the northwestern rift flank where crustal thickness is 36–42 km and average crustal $V_p/V_s$ is 1.80–1.88; (2) ~85 km including the rift valley where crustal thickness is 33–36 km and average crustal $V_p/V_s$ is 1.84–1.92; (3) ~35 km of the southeastern rift flank, adjacent to the rift valley, where crustal thickness and average crustal $V_p/V_s$ changes from 37 to 40 km and 1.85 to 1.78;

and (4) ~100 km of the southeastern rift flank where crustal thickness is 37–41 km and average crustal $V_p/V_s$ is 1.74–1.82.

[65] 5. The crust beneath the rift valley can be subdivided into northwestern and southeastern rift sectors. The thinnest crust (with a clear Moho at ~32 km) and highest $V_p/V_s$ values occur in the northwestern sector, suggesting crustal thinning and a strong likelihood of partially molten rocks. In conjunction with gravity and geochemical studies, the crust in the northwestern rift sector is interpreted to have a poorly developed magma system, containing less intrusive magma than the crust in the southeastern rift sector, where high velocity and density anomalies and a Moho "hole" constrain the limits of a well-developed magma system, consisting of upper crustal magma chambers, midcrustal intense gabbroic diking and lower crustal sills.

[66] 6. Moderately elevated $V_p/V_s$ (1.80–1.88) show that the crust beneath the Ethiopian plateau (northwestern rift flank) consists of some mafic material and, when combined with magnetotelluric results, suggests that a mafic middle and lower crust may be overlain by a felsic upper crust. The most notable feature of the crust of the northwestern rift flank is a thick (6–18 km), high $P$ wave velocity (7.3–7.7 km/s) lower crustal layer (NWLCL).

[67] 7. The upper and lower depth limits of the NWLCL are constrained to be 27–31 km and 36–48 km, respectively, with the thinnest parts occurring toward the northwestern rift margin, indicating that rifting occurred where thickening due to magmatic intrusion had probably strengthened the crust by the least amount across the profile (assuming the majority of the NWLCL had been emplaced prior to rifting).

[68] 8. $V_p/V_s$ is modeled to be high (1.85–1.93) within the NWLCL and is interpreted to be composed of frozen gabbroic sills (which may also contain some partial melt), supported by knowledge obtained from seismic reflection/wide-angle refraction, gravity and geochemical studies. A gradational upper boundary and inferred layered internal structure suggest that the NWLCL was formed by repeated intrusions into the lower crust, which may have partially melted existing lower crustal rocks and/or partially crystallized to contribute to the observed bimodal prerift and synrift volcanism.

[69] 9. Average crustal $V_p/V_s$ of 1.70–1.77 suggest that the crust beneath the southeastern rift flank is felsic to intermediate in composition, with a crustal thickness range of between 37 and 41 km and no clear geophysical evidence for concentrated magmatic intrusion. A ~35 km wide transition zone marks the change from the intruded (and probably thinned) crust beneath the rift to the amagmatic thick crust of the southeastern rift flank, in which average crustal $V_p/V_s$ decrease by ~0.07 and crustal thicknesses increase by ~5 km.

## Acknowledgments

[70] The Ethiopia-Afar Geoscientific Lithospheric Experiment (EAGLE) was funded by the NERC, U.K.; the U.S. NSF Continental Dynamics Program; the Texas Higher Education Coordinating Board; the Royal Society; and the University of Leicester. Deployment of the EAGLE phase III seismometers was completed by Graeme Mackenzie, James Blight, Paul Denton, Alex Brisbourne, Kifle Damtew, Kimemu Nurie, Ewenet Gasawbeza, and Ethio-Der drivers. We wish to sincerely thank Atalay Ayele and Laike Asfaw of the Geophysical Observatory, Addis Abeba University, and all of the Ethiopian officials, schools and local people for their cooperation. All at SEIS-UK are thanked for providing the instrumentation, data storage, and technical advice. We are indebted to Derek Keir and reviewers Cindy Ebinger and Christel Tiberi for their constructive comments, which greatly improved the manuscript. The seismological data were analyzed using SAC [e.g., *Goldstein and Snoke*, 2005]. Figure 1 was adapted from the original using Illustrator. Figures 3, 4, 6, and 9 were made with GMT [*Wessel and Smith*, 1995] and then modified/labeled using Adobe Illustrator. Figures 5, 7, and 8 were made with GMT only.

## References

Abdelsalam, M. G., and R. J. Stern (1996), Sutures and shear-zones in the Arabian-Nubian Shield, *J. Afr. Earth Sci.*, *23*(3), 289–310.

Abebe, T., P. Manetti, M. Bonini, G. Corti, F. Innocenti, and F. Mazzarini (2005), Geological map of the northern Main Ethiopian Rift and its implications for the volcano-tectonic evolution of the rift, *Map Chart Ser.*, *MCH094*, scale 1:200,000, doi:10.1130/2005MCH094TXT, Geol. Soc. of Am., Boulder, Colo.

Acocella, V., and T. Korme (2002), Holocene extension direction along the Main Ethiopian Rift, East Africa, *Terra Nova*, *14*(3), 191–197.

Ammon, C. J. (1991), The isolation of receiver function effect from teleseismic *P* waveforms, *Bull. Seismol. Soc. Am.*, *81*(6), 2504–2510.

Annen, C., and R. S. J. Sparks (2002), Effects of repetitive emplacement of basaltic intrusions on thermal evolution and melt generation in the crust, *Earth Planet. Sci. Lett.*, *203*, 937–955.

Ayalew, D., and G. Yirgu (2003), Crustal contribution to the genesis of Ethiopian plateau rhyolitic ignimbrites: Basalt and rhyolite geochemical provinciality, *J. Geol. Soc. London*, *160*, 47–56.

Ayalew, D., P. Barbey, B. Marty, L. Reisberg, G. Yirgu, and R. Pik (2002), Source, genesis and timing of giant ignimbrite

deposits associated with Ethiopian continental flood basalts, *Geochim. Cosmochim. Acta*, *66*, 1429–1448.

Ayele, A., G. Stuart, and J. M. Kendall (2004), Insights into rifting from shear wave splitting and receiver functions: An example from Ethiopia, *Geophys. J. Int.*, *157*(1), 354–362.

Bastow, I. D. (2005), Upper-mantle seismic structure in a region of incipient continental break-up: Northern Ethiopian Rift, Ph.D. thesis, Univ. of Leeds, Leeds, U. K.

Bastow, I. D., G. W. Stuart, J.-M. Kendall, and C. J. Ebinger (2005), Upper mantle seismic structure in a region of incipient continental breakup: Northern Ethiopian Rift, *Geophys. J. Int.*, *162*, 479–493.

Bastow, I. D., A. A. Nyblade, G. W. Stuart, T. O. Rooney, and M. H. Benoit (2008), Upper mantle seismic structure beneath the Ethiopian hotspot: Rifting at the edge of the African low-velocity anomaly, *Geochem. Geophys. Geosyst.*, *9*, Q12022, doi:10.1029/2008GC002107.

Benoit, M. H., A. A. Nyblade, T. J. Owens, and G. W. Stuart (2006a), Mantle transition zone structure and upper mantle S velocity variations beneath Ethiopia: Evidence for a broad, deep-seated thermal anomaly, *Geochem. Geophys. Geosyst.*, *7*, Q11013, doi:10.1029/2006GC001398.

Benoit, M. H., A. A. Nyblade, and J. C. VanDecar (2006b), Upper mantle *P*-wave speed variations beneath Ethiopian and the origin of the Afar hotspot, *Geology*, *34*(5), 329–332.

Bergantz, G. W. (1989), Underplating and partial melting: Implications for melt generation and extraction, *Science*, *245*, 1093–1095.

Berhe, S. M. (1990), Ophiolites in northeast and East Africa—Implications for proterozoic crustal growth, *J. Geol. Soc.*, *147*, 41–57.

Bilham, R., R. Bendick, K. Larson, P. Mohr, J. Braun, S. Tesfaye, and L. Asfaw (1999), Secular and tidal strain across the main Ethiopian rift, *Geophys. Res. Lett.*, *26*(18), 2789–2792.

Birt, C. (1996), Geophysical investigation of active continental rifting in southern Kenya, Ph.D. thesis, Univ. of Leicester, Leicester, U. K.

Birt, C. S., P. K. H. Maguire, M. A. Khan, H. Thybo, G. R. Keller, and J. Patel (1997), The influence of pre-existing structures on the evolution of the southern Kenya Rift Valley—Evidence from seismic and gravity studies, *Tectonophysics*, *278*(1–4), 211–242.

Boccaletti, M., R. Mazzuoli, M. Bonini, T. Trua, and B. Abebe (1999), Plio-Quaternary volcanotectonic activity in the northern sector of the Main Ethiopian Rift: Relationships with oblique rifting, *J. Afr. Earth Sci.*, *29*(4), 679–698.

Cassidy, J. (1992), Numerical experiments in broadband receiver function analysis, *Bull. Seismol. Soc. Am.*, *82*(3), 1453–1474.

Castagna, J. P., M. L. Batzle, and R. L. Eastwood (1985), Relationships between compressional-wave and shear-wave velocities in clastic silicate rocks, *Geophysics*, *50*(4), 571–581.

Chernet, T., W. K. Hart, J. L. Aronson, and R. C. Walter (1998), New age constraints on the timing of volcanism and tectonism in the northern Main Ethiopian Rift–southern Afar transition zone (Ethiopia), *J. Volcanol. Geotherm. Res.*, *80*(3–4), 267–280.

Christensen, N. I. (1996), Poisson's ratio and crustal seismology, *J. Geophys. Res.*, *101*(B2), 3139–3156.

Christensen, N. I., and W. D. Mooney (1995), Seismic velocity structure and composition of the continental crust: A global view, *J. Geophys. Res.*, *100*(B6), 9761–9788.

Chu, D. H., and R. G. Gordon (1999), Evidence for motion between Nubia and Somalia along the southwest Indian Ridge, *Nature*, *398*, 64–67.

Cornwell, D. G. (2008), Magma-assisted continental rift margins: The Ethiopian rift, Ph.D. thesis, Univ. of Leicester, Leicester, U. K.

Cornwell, D. G., G. D. Mackenzie, P. K. H. Maguire, R. W. England, L. M. Asfaw, and B. Oluma (2006), Northern Main Ethiopian Rift crustal structure from new high-precision gravity data, in *The Afar Volcanic Province Within the East African Rift System*, edited by G. Yirgu, C. J. Ebinger, and P. K. H. Maguire, *Geol. Soc. Spec. Publ.*, *258*, 307–321.

Coulie, E., X. Quidelleur, P. Y. Gillot, V. Courtillot, J. C. Lefevre, and S. Chiesa (2003), Comparative K-Ar and Ar/Ar dating of Ethiopian and Yemenite Oligocene volcanism: Implications for timing and duration of the Ethiopian traps, *Earth Planet. Sci. Lett.*, *206*(3–4), 477–492.

Daly, E., D. Keir, C. J. Ebinger, G. W. Stuart, I. D. Bastow, and A. Ayele (2008), Crustal tomographic imaging of a transitional continental rift: The Ethiopian rift, *Geophys. J. Int.*, *172*, 1033–1048, doi:10.1111/j.1365–246X.2007.03682.x.

Dow, D. B., M. Beyth, and T. Hailu (1971), Palaeozoic glacial rocks recently discovered in northern Ethiopia, *Geol. Mag.*, *108*(1), 53–60.

Dugda, M. T., and A. A. Nyblade (2006), New constraints on crustal structure in eastern Afar from the analysis of receiver functions and surface wave dispersion in Djibouti, in *The Afar Volcanic Province within the East African Rift System*, edited by G. Yirgu, C. J. Ebinger, and P. K. H. Maguire, *Geol. Soc. Spec. Publ.*, *259*, 239–251.

Dugda, M. T., A. A. Nyblade, J. Julia, C. A. Langston, C. J. Ammon, and S. Simiyu (2005), Crustal structure in Ethiopia and Kenya from receiver function analysis: Implications for rift development in eastern Africa, *J. Geophys. Res.*, *110*, B01303, doi:10.1029/2004JB003065.

Dunbar, J. A., and D. S. Sawyer (1989), How preexisting weaknesses control the style of continental breakup, *J. Geophys. Res.*, *94*, 7278–7298.

Ebinger, C. J., and M. Casey (2001), Continental breakup in magmatic provinces: An Ethiopian example, *Geology*, *29*(6), 527–530.

Ebinger, C. J., T. Yemane, G. Woldegabriel, J. L. Aronson, and R. C. Walter (1993), Late Eocene-Recent volcanism and faulting in the southern Main Ethiopian Rift, *J. Geol. Soc.*, *150*, 99–108.

Furman, T., J. Bryce, T. Rooney, B. Hanan, G. Yirgu, and D. Ayalew (2006), Heads and tails: 30 million years of the Afar plume, in *The Afar Volcanic Province within the East African Rift System*, edited by G. Yirgu, C. J. Ebinger, and P. K. H. Maguire, *Geol. Soc. Spec. Publ.*, *259*, 95–119.

Gani, N. D. S., M. R. Gani, and M. G. Abdelsalam (2007), Blue Nile incision on the Ethiopian Plateau: Pulsed plateau growth, Pliocene uplift, and hominin evolution, *GSA Today*, *17*(9), 4–11, doi:10.1130/GSAT01709A.1.

Garland, C. R. (1972), Explanation of the geological map of the Adigrat sheet (ND 37-2) (scale 1:250,000), technical report, Ethiopian Inst. of Geol. Surv., Addis Ababa.

Gashawbeza, E. M., S. L. Klemperer, A. A. Nyblade, K. T. Walker, and K. M. Keranen (2004), Shear-wave splitting in Ethiopia: Precambrian mantle anisotropy locally modified by Neogene rifting, *Geophys. Res. Lett.*, *31*, L18602, doi:10.1029/2004GL020471.

Goldstein, P., and A. Snoke (2005), SAC availability for the IRIS community (online), *IRIS DMS Newsl.*, *7*(1). (Available at http://www.iris.edu/news/newsletter)

Harland, K. E., R. S. White, and H. Soosalu (2009), Crustal structure beneath the Faroe Islands from teleseismic receiver functions, *Geophys. J. Int.*, *177*, 115–124, doi:10.1111/j.1365–246X.2008.04018.x.

Hofmann, C., V. Courtillot, G. Feraud, P. Rochette, G. Yirgu, E. Ketefo, and R. Pik (1997), Timing of the Ethiopian flood basalt event and implications for plume birth and global change, *Nature*, *389*(6653), 838–841.

Huismans, R. S., and C. Beaumont (2007), The Iberia-Newfoundland continental extensional system (dynamic modelling), in *Imaging, Mapping and Modelling Continental Lithosphere Extension and Breakup*, edited by G. D. Karner, G. Manatschal, and L. M. Pinheiro, *Geol. Soc. Spec. Publ.*, *282*, 111–138.

Huppert, H. E., and R. S. J. Sparks (1988), The generation of granitic magmas by intrusion of basalt into continental crust, *J. Petrol.*, *29*(3), 599–624.

Johnson, P. R., and B. Woldehaimanot (2003), Development of the Arabian-Nubian Shield: Perspectives on accretion and deformation in the northern East African Orogen and the assembly of Gondwana, in *Proterozoic East Gondwana: Supercontinent Assembly and Breakup*, edited by M. Yoshida, B. F. Windley, and S. Dasgupta, *Geol. Soc. Spec. Publ.*, *206*, 289–325.

Jones, C. H., B. P. Wernicke, G. L. Farmer, J. D. Walker, D. S. Coleman, L. W. McKenna, and F. V. Perry (1992), Variations across and along a major continental rift: An interdisciplinary study of the Basin and Range Province, western USA, *Tectonophysics*, *213*, 57–96.

Kazmin, V. (1975), Explanatory note to the geology of Ethiopia, technical report, Ethiopian Inst. of Geol. Surv., Addis Ababa.

Keir, D., I. D. Bastow, K. A. Whaler, E. Daly, D. G. Cornwell, and S. Hautot (2009), Lower crustal earthquakes near the Ethiopian rift induced by magmatic processes, *Geochem. Geophys. Geosyst.*, *10*, Q0AB02, doi:10.1029/2009GC002382.

Kennett, B. (1983), *Seismic Wave Propagation in Stratified Media*, Cambridge Univ. Press, Cambridge, U. K.

Kennett, B., and E. R. Engdahl (1991), Traveltimes for global earthquake location and phase identification, *Geophys. J. Int.*, *105*, 429–465.

Keranen, K., and S. L. Klemperer (2008), Discontinuous and diachronous evolution of the Main Ethiopian Rift: Implications for development of continental rifts, *Earth Planet. Sci. Lett.*, *265*, 96–111.

Keranen, K. M., S. L. Klemperer, R. Gloaguen, and the EAGLE Working Group (2004), Imaging a proto-ridge axis in the Main Ethiopian Rift, *Geology*, *32*(11), 949–952.

Kieffer, B., et al. (2004), Flood and shield basalts from Ethiopia: Magmas from the African Superswell, *J. Petrol.*, *45*(4), 793–834.

Korme, T., V. Acocella, and B. Abebe (2004), The role of pre-existing structures in the origin, propagation and architecture of faults in the main Ethiopian rift, *Gondwana Res.*, *7*(2), 467–479.

Kusznir, N. J., and R. G. Park (1987), The extensional strength of the continental lithosphere: Its dependence on geothermal gradient and crustal composition and thickness, in *Continental Extension Tectonics*, edited by M. P. Coward, J. F. Dewey, and P. L. Hancock, *Geol. Soc. Spec. Publ.*, *28*, 22–52.

Langston, C. A. (1977), The effect of planar dipping structure on source and receiver responses for constant ray parameter, *Bull. Seismol. Soc. Am.*, *67*(4), 1029–1050.

Levin, V., and J. Park (1997), $P - SH$ conversions in a flat-layered medium with anisotropy of arbitrary orientation, *Geophys. J. Int.*, *131*, 253–266.

Mackenzie, G. D., H. Thybo, and P. K. H. Maguire (2005), Crustal velocity structure across the Main Ethiopian Rift: Results from two-dimensional wide-angle seismic modelling, *Geophys. J. Int.*, *162*, 994–1006.

Maguire, P. K. H., et al. (2003), Geophysical project in Ethiopia studies continental breakup, *Eos Trans. AGU*, *84*(337), 342–343.

Maguire, P. K. H., et al. (2006), Crustal structure of the northern Main Ethiopian Rift from the EAGLE controlled-source survey: A snapshot of incipient lithospheric break-up, in *The Afar Volcanic Province within the East African Rift System*, edited by G. Yirgu, C. J. Ebinger, and P. K. H. Maguire, *Geol. Soc. Spec. Publ.*, *259*, 269–291.

Mahatsente, R., G. Jentzsch, and T. Jahr (1999), Crustal structure of the Main Ethiopian Rift from gravity data: 3-dimensional modeling, *Tectonophysics*, *313*(4), 363–382.

McClusky, S., R. Reilinger, S. Mahmoud, D. Ben Sari, and A. Tealeb (2003), GPS constraints on Africa (Nubia) and Arabia plate motions, *Geophys. J. Int.*, *155*, 126–138.

Mohr, P. (1983), Ethiopian flood-basalt province, *Nature*, *303*(5918), 577–584.

Owens, T. J., and G. Zandt (1997), Implications of crustal property variations for models of Tibetan Plateau, *Nature*, *387*, 37–43.

Pik, R., C. Deniel, C. Coulon, G. Yirgu, and B. Marty (1999), Isotopic and trace element signatures of Ethiopian flood basalts: Evidence for plime-lithosphere interactions, *Geochim. Cosmochim. Acta*, *63*, 2263–2279.

Pik, R., B. Marty, J. Carignan, and J. Lave (2003), Stability of the Upper Nile drainage network (Ethiopia) deduced from (U-Th)/He thermochronometry: Implications for uplift and erosion of the Afar plume dome, *Earth Planet. Sci. Lett.*, *215*(1–2), 73–88.

Rochette, P., E. Tamrat, G. Féraud, R. Pik, V. Courtillot, E. Ketefo, C. Coulon, C. Hofmann, D. Vandamme, and G. Yirgu (1998), Magnetostratigraphy and timing of the Oligocene Ethiopian traps, *Earth Planet. Sci. Lett.*, *164*, 497–510.

Rooney, T. T., T. Furman, G. Yirgu, and D. Ayalew (2005), Structure of the Ethiopian lithosphere: Evidence from mantle xenoliths, *Geochim. Cosmochim. Acta*, *69*(15), 3889–3910, doi:10.1016/j.gca.2005.03.043.

Rooney, T., T. Furman, I. D. Bastow, D. Ayalew, and G. Yirgu (2007), Lithospheric modification during crustal extension in the Main Ethiopian Rift, *J. Geophys. Res.*, *112*, B10201, doi:10.1029/2006JB004916.

Stern, R. J. (1994), Arc assembly and continental collision in the Neoproterozoic east African Orogen: Implication for the consolidation of Gondwanaland, *Annu. Rev. Earth Planet. Sci.*, *22*, 319–351.

Stuart, G., I. D. Bastow, and C. J. Ebinger (2006), Crustal structure of the northern Main Ethiopian Rift from receiver function studies, in *The Afar Volcanic Province Within the East African Rift System*, edited by G. Yirgu, C. J. Ebinger, and P. K. H. Maguire, *Geol. Soc. Spec. Publ.*, *259*, 253–267.

Tefera, M., T. Chernet, and W. Haro (1996), Explanation of the geological map of Ethiopia (scale 1:2,000,000), technical report, Ethiopian Inst. of Geol. Surv., Addis Ababa.

Thybo, H., and C. A. Nielsen (2009), Magma-compensated crustal thinning in continental rift zones, *Nature*, *457*, 873–876.

Thybo, H., P. K. H. Maguire, C. Birt, and E. Perchuc (2000), Seismic reflectivity and magmatic underplating beneath the Kenya Rift, *Geophys. Res. Lett.*, *27*(17), 2745–2748.

Tiberi, C., C. J. Ebinger, V. Ballu, G. W. Stuart, and B. Oluma (2005), Inverse models of gravity data from the Red Sea-Aden-East African rifts triple junction zone, *Geophys. J. Int.*, *163*(2), 775–787, doi:10.1111/j.1365–246X.2005.02710.x.

Tomlinson, J., P. Denton, P. Maguire, and D. Booth (2006), Analysis of the crustal velocity structure of the British Isles using teleseismic receiver functions, *Geophys. J. Int.*, *167*, 223–237.

Tommasi, A., and A. Vauchez (2001), Continental rifting parallel to ancient collisional belts: An effect of the mechanical anisotropy of the lithospheric mantle, *Earth Planet. Sci. Lett.*, *185*, 199–210.

van Wijk, J. W., and D. K. Blackman (2005), Dynamics of continental rift propagation: The end-member modes, *Earth Planet. Sci. Lett.*, *229*, 247–258.

Watanabe, T. (1993), Effects of water and melt on seismic velocities and their application to characterization of seismic reflectors, *Geophys. Res. Lett.*, *20*, 2933–2936.

Wessel, P., and W. H. F. Smith (1995), New version of the generic mapping tools released, *Eos Trans. AGU*, *76*, 329.

Whaler, K. A., and S. Hautot (2006), Magnetotelluric studies of the northern Ethiopian Rift (EAGLE phase III), in *The Afar Volcanic Province Within the East African Rift System*, edited by G. Yirgu, C. J. Ebinger, and P. K. H. Maguire, *Geol. Soc. Spec. Publ.*, *259*, 293–305.

White, R. S., L. K. Smith, A. W. Roberts, P. A. F. Christie, N. J. Kusznir, and iSIMM Team (2008), Lower-crustal intrusion in the North Atlantic continental margin, *Nature*, *452*, 460–464.

Whittington, A. G., A. M. Hofmeister, and P. I. Nabelek (2009), Temperature-dependent thermal diffusivity of the Earth's crust and implications for magmatism, *Nature*, *458*, 319–321.

Wilson, D., R. Aster, J. Ni, S. Grand, M. West, W. Gao, W. Baldridge, and S. Semken (2005), Imaging the seismic structure of the crust and upper mantle beneath the Great Plains, Rio Grande Rift, and Colorado Plateau using receiver functions, *J. Geophys. Res.*, *110*, B05306, doi:10.1029/2004JB003492.

WoldeGabriel, G., J. L. Aronson, and R. C. Walter (1990), Geology, geochronology, and rift basin development in the central sector of the Main Ethiopia Rift, *Geol. Soc. Am. Bull.*, *102*(4), 439–458.

Woldetinsae, G., and H.-J. Götze (2005), Gravity field and isostatic state of Ethiopia and adjacent areas, *J. Afr. Earth Sci.*, *41*, 103–117.

Wolfenden, E., C. Ebinger, G. Yirgu, A. Deino, and D. Ayalew (2004), Evolution of the northern Main Ethiopian Rift: Birth of a triple junction, *Earth Planet. Sci. Lett.*, *224*(1–2), 213–228.

Yihunnie, T., and M. Tesfaye (2002), Structural evidence for the allochthonous nature of the Bulbul terrane in southern Ethiopia: A west-verging thrust nappe, *J. Afr. Earth Sci.*, *34*, 85–93.

Zandt, G., H. Gilbert, T. J. Owens, M. Ducea, J. Saleeby, and C. H. Jones (2004), Active foundering of a continental arc root beneath the southern Sierra Nevada in California, *Nature*, *431*, 41–46.

Zhu, L., and H. Kanamori (2000), Moho depth variation in southern California from teleseismic receiver functions, *J. Geophys. Res.*, *105*(B2), 2969–2980.